

# Angular Normalization of Land Surface Temperature and Emissivity Using Multiangular Middle and Thermal Infrared Data

Huazhong Ren, Rongyuan Liu, Guangjian Yan, Xihan Mu, Zhao-Liang Li, Françoise Nerry, and Qiang Liu

**Abstract**—This paper aimed at the case of nonisothermal pixels and proposed a daytime temperature-independent spectral indices (TISI) method to retrieve directional emissivity and effective temperature from daytime multiangular observed images in both middle and thermal infrared (MIR and TIR) channels by combining the kernel-driven bidirectional reflectance distribution function (BRDF) model and the TISI method. Four groups of angular observations and two groups of MIR and TIR channels with narrow and broad bandwidths were used to investigate the influence of angular observations and bandwidth on the retrieval accuracy. Model sensitivity analysis indicated that the new method can generally obtain directional emissivity and temperature with an error less than 0.015 and 1.5 K if the noise included in the measured directional brightness temperature (DBT) and atmospheric data was no more than 1.0 K and 10%, respectively. The analysis also indicated that 1) large-angle intervals among the angular observations and a larger viewing zenith angle, with respect to nadir direction, can improve the retrieval accuracy because those angle conditions can result in significant difference for components' fractions and DBT under different viewing directions; 2) narrow channels can produce better results than broad channels. The new method was finally applied to a multiangular MIR

and TIR data set acquired by an airborne system, and a modified kernel-driven BRDF model was used for angular normalization to the surface temperature for the first time. The difference of the retrieved emissivity and Advanced Spaceborne Thermal Emission and Reflection Radiometer (ASTER) emissivity was found to be approximately 0.012 in the study area.

**Index Terms**—Bidirectional reflectance distribution function (BRDF) model, directional effective temperature, directional emissivity, multiangular thermal remote sensing, temperature-independent spectral indices (TISI).

## I. INTRODUCTION

LAND surface temperature (LST) is strongly required for many applications, including agrometeorology, climate, and environmental studies [1]–[3]. Thermal infrared (TIR) images from aircraft and spaceborne satellites provide a unique opportunity to map this parameter at regional and even global scales. However, the determination of LST from remotely sensed data needs to solve two types of problems. The first is atmospheric correction, which aims to remove the contribution of atmospheric emission and scattering to the target radiation in the path from the surface to the sensor. The other involves accounting for the emissivity effect on the LST to allow the retrieval of LST from the radiance measured at the surface. Many methods have been proposed to retrieve LST from remotely sensed data depending on different specifications of TIR sensors and the atmospheric and emissivity data situations, and these methods can be roughly grouped into three categories: the single-channel algorithm [4], [5], multichannel methods (e.g., the split-window algorithm [6]–[8] and the temperature and emissivity separation (TES) method [9]), and the multi-time methods (e.g., the temperature-independent spectral indices (TISI) method [10], the two-temperature method [11], [12], and the physical day and night algorithm [13]). Some algorithms were also proposed to retrieve both LST and emissivity from hyperspectral TIR data, such as the iterative spectrally smooth temperature-emissivity separation [14] and alpha-driven emissivity method [15]. For operational purposes, the aforementioned methods often take the observed pixel as a homogeneous and isothermal target. This assumption is reasonable for pure or quasi-pure pixels, such as bare soil, sand, snow, and dense vegetated surface. However, for mixed pixels including two or more components at different temperatures and emissivities, the temperature actually presents spectral and angular variations. As a result, the aforementioned assumption will be incorrect,

Manuscript received May 13, 2013; revised July 27, 2013; accepted September 30, 2013. This work was supported by China 973 program (Grant No. 2013CB733402), the key program of NSFC (Grant 41331171, 41230747, and 41231170), and China 863 program (Grant 2012AA12A304 and 2012AA12A303). (Corresponding author: G. Yan.)

H. Ren is with the State Key Laboratory of Remote Sensing Science, School of Geography, Beijing Normal University, Beijing 100875, China, the Institute of Remote Sensing and Geographic Information System, Peking University, Beijing 100871, China, and also with ICube, Université de Strasbourg, 67412 Illkirch, France (e-mail: renhuazhong@mail.bnu.edu.cn).

R. Liu is with the State Key Laboratory of Remote Sensing Science, School of Geography, Beijing Normal University, Beijing 100875, China, and also with ICube, Université de Strasbourg, 67412 Illkirch, France (e-mail: rongyuanliu@mail.bnu.edu.cn).

G. Yan and X. Mu are with the State Key Laboratory of Remote Sensing Science, School of Geography, Beijing Normal University, Beijing 100875, China (e-mail: gjyan@bnu.edu.cn; muxihan@bnu.edu.cn).

Z.-L. Li is with the Key Laboratory of Agri-informatics, Ministry of Agriculture/Institute of Agricultural Resources and Regional Planning, Chinese Academy of Agricultural Sciences, Beijing 100081, China, and also with ICube, Université de Strasbourg, 67412 Illkirch, France (e-mail: lizhaoliang@caas.cn; lizl@unistra.fr).

F. Nerry is with ICube, Université de Strasbourg, 67412 Illkirch, France (e-mail: f.nerry@unistra.fr).

Q. Liu is with the College of Global Change and Earth System Science, Beijing Normal University, Beijing 100875, China, and also with the Institute of Remote Sensing and Digital Earth, Chinese Academy of Sciences, Beijing 100094, China (e-mail: liuqiang@irsa.ac.cn).

Color versions of one or more of the figures in this paper are available online at <http://ieeexplore.ieee.org>.

Digital Object Identifier 10.1109/TGRS.2013.2285924

and at least, the retrieved LST only presents the effective temperature at its corresponding viewing direction and cannot be directly taken as the temperature at nadir or under other directions in theory.

The angular behavior of LST has been investigated in many previous studies [16]–[23], and this angular variation results primarily from the angular variation of the pixel emissivity for 3-D surfaces and the relative weights of more than one component (e.g., vegetation and background soil) with different temperatures included in the scene. Some ground measurements have indicated that the LST difference at nadir and off-nadir observations can be as large as 5 K for bare soils and even 10 K for urban areas. For satellite images, the pixels also face a similar situation because the pixels in the same image are usually observed with significantly different viewing angles. For example, the Moderate Resolution Imaging Spectroradiometer (MODIS) scans the land surface in the cross-track direction with viewing zenith angle (VZA) varying from  $-65^\circ$  to  $+65^\circ$ , and thus, angle-dependent variations in the retrieved LST are inevitable, which make the LSTs of different pixels in the same image incomparable and eventually lead to large errors. Similar cases can be observed in other satellite sensors, such as Advanced Very High Resolution Radiometer (AVHRR), Spinning Enhanced Visible and InfraRed Imager (SEVIRI), and so on. Therefore, it is crucial to make angular corrections to the LST [30].

Until recently, there have been two types of methods for solving this angular LST problem. One method focused on the modeling of directional emissivity, and the other method is aimed at the retrieval of pixel components' temperatures. The former simply attributes the angular variation of the measured effective temperature to the directional behavior of the pixel emissivity. If the directional emissivity at the viewing direction is known, LST can be retrieved by taking the inverse of the radiative transfer model, and the result is consequently assumed to be angle independent [22]. However, because this method ignores the angular variation caused by the components' temperatures and it is always difficult to determine the directional emissivity at the pixel scale, the results of this method are far from satisfactory. In contrast, the retrieval of components' temperatures is more promising for achieving LST angular correction because once the components' temperatures are obtained from multiangle observations [24]–[26], vegetation indices [27], or spatial patterns [28], the thermal radiance at any direction can be theoretically calculated by weighting the components' temperatures with their corresponding fractions. However, this method always requires the components' emissivities and their fractions to be known in advance, but those parameters are seldom easily obtained in practice. As a result, there has been no practical way until now to perform LST angular correction due to the complexity of this issue. Multiangular observation on the same targets is considered the most promising way to solve this problem. However, there are still rare reports of LST angular correction or simultaneous retrieval of directional emissivity and temperature from multiangular TIR images because no more than two angular observations were designed for the current satellite sensors [e.g., the Advanced Along Track Scanning Radiometer (ATSR/AATSR)], and the number of the observa-

tion was less than that of the unknowns. On the other hand, more angular observations can be obtained easier from airborne sensors than from spaceborne sensors, such as the Wide-angle infrared Dual-mode line/area Array Scanner (WiDAS) system [27] in the Watershed Allied Telemetry Experimental Research (WATER) campaign [29]. From this viewpoint, the objective of this paper is to develop a new method for simultaneously retrieving directional emissivity and temperature from the multiangular image of middle infrared (MIR) and TIR channels and to achieve angular correction to the temperature using the TISI method and the kernel-driven bidirectional reflectance distribution function (BRDF) model. It is organized as follows: Section II will present some basic theory on retrieval of emissivity and temperature data from multiangular observations in both MIR and TIR channels; Section III will address the model sensitivity analysis with respect to some input parameters and errors; Section IV will be devoted to the application of the new method to an aircraft data set consisting of MIR and TIR images at several viewing angles, which were obtained in the WATER campaign [29], and the cross-validation of the results; and finally, some conclusions and discussions will be stated in the last section of this paper.

## II. ALGORITHM FOR RETRIEVING ANGULAR TEMPERATURE AND EMISSIVITY

### A. Radiative Transfer Equation

For a cloud-free sky, the radiance measured by an infrared channel of a sensor onboard a satellite or an aircraft can be approximated as follows [30]:

$$I(\theta_s, \theta_v, \varphi) = R(\theta_s, \theta_v, \varphi) \cdot \tau(\theta_s, \theta_v, \varphi) + R_{a\uparrow} + R_{s1\uparrow}. \quad (1)$$

The first term on the right-hand side of (1) is the measured surface-leaving radiance after attenuation passing through the atmosphere, and the second and third terms are the contribution of upward atmospheric emission  $R_{a\uparrow}$  and scattered solar radiance  $R_{s1\uparrow}$ , respectively. The surface-leaving radiance  $R(\theta_s, \theta_v, \varphi)$  is written as the following:

$$R(\theta_s, \theta_v, \varphi) = \varepsilon(\theta_v, \varphi_v) B [T(\theta_s, \theta_v, \varphi)] + [1 - \varepsilon(\theta_v, \varphi_v)] \cdot (R_{a\downarrow} + R_{s1\downarrow}) + \rho(\theta_s, \theta_v, \varphi) \cdot E_{\text{sun}} \quad (2)$$

where  $\theta_v$  and  $\theta_s$  are the VZA and solar zenith angle (SZA), respectively, whereas  $\varphi$  is the relative azimuth angle between the viewing azimuth angle  $\varphi_v$  (VAA) and solar azimuth angles  $\varphi_s$  (SAA).  $\tau$  is the atmospheric transmittance. This first term on the right-hand side of (2) is the surface thermal radiation, whereas  $\varepsilon(\theta_v, \varphi_v)$  is the surface emissivity in the viewing direction. Because the emissivity is assumed to be VAA-independent in this paper, as reported in [21], [31], and [32], the term  $\varepsilon(\theta_v, \varphi_v)$  will be replaced with  $\varepsilon(\theta_v)$  in the following discussion.  $B[T(\theta_s, \theta_v, \varphi)]$  is the surface thermal emission calculated using Planck's law at the equivalent temperature  $T(\theta_s, \theta_v, \varphi)$ , which varies with the viewing geometry for the nonisothermal pixel rather than an angle-independent value, as indicated in some previous studies. The second term is the downward atmospheric radiance  $R_{a\downarrow}$  and solar scattering radiance  $R_{s1\downarrow}$ , which are reflected by the surface at the viewing direction. The last

part of (2) presents the solar direct illumination reflected by the surface with the bidirectional reflectivity  $\rho(\theta_s, \theta_v, \varphi)$ . For the MIR channel at nighttime and the TIR channel, no reflected solar radiance [ $R_{sl} \downarrow$  and  $E_{sun}$  in (2)] contributes to the surface-leaving radiance.

### B. Daytime TISI Method

The TISI method was initially developed to separate temperature and emissivity from daytime and nighttime MIR and TIR images, and the method has been successfully applied to retrieve bidirectional reflectivity in the MIR channel and emissivity from the AVHRR, MODIS, and SEVIRI onboard Meteosat Second Generation satellite [33]–[36]. According to the TISI method, Planck's law can be approximated using an exponent function for the MIR or TIR channel as follows:

$$L = \varepsilon \cdot m \cdot T^n \quad (3)$$

where the coefficients  $m$  and  $n$  are channel dependent. Furthermore, the surface-leaving radiance can be consequently expressed as  $R = \varepsilon \cdot m \cdot T^n \cdot C$ , with  $C$  accounting for the reflected downward atmospheric radiations. A two-channel emissivity ratio  $TISIE_{ij}$  between one MIR channel (denoted by  $i$ ) without solar illumination and one TIR channel (denoted by  $j$ ) was defined in [34] and [37], to improve the retrieval of emissivity and consequently LST as follows:

$$TISIE_{ij} = \frac{\varepsilon_i}{\varepsilon_j} = \frac{R'_i}{R'_j} \cdot \frac{m_j^{n_{ij}}}{m_i} \cdot \frac{C_j^{n_{ij}}}{C_i} = \frac{R'_i}{R'_j} \cdot M_{ji} \cdot C_{ji} \quad (4a)$$

with  $n_{ij} = n_i/n_j$

$$R'_i = TISIE_{ij} \cdot R'_j \cdot M_{ij} \cdot C_{ij} \quad (4b)$$

where  $R'_i$  is the surface-emitted radiance in the MIR channel without solar illumination, whereas  $R'_j$  is for the TIR channel. Introducing (4b) into (2) obtains the expression to calculate the bidirectional reflectivity as follows:

$$\rho_i(\theta_s, \theta_v, \varphi) = \frac{1}{E_{sun}} [R_i - TISIE_{ij} \cdot R'_j \cdot M_{ij} \cdot C_{ij}]. \quad (5)$$

The final solution of (5) requires the value of  $TISIE_{ij}$ , which is assumed to be the same at daytime and nighttime if there is no occurrence of rain, snow, or dew, and the nighttime  $TISIE_{ij}$  can be calculated directly using (4a) from the nighttime observations in both the MIR and TIR channels. However, because the TISI method requires daytime and nighttime observations of the same target in a short time frame, its application cannot be achieved for sensors that only provide daytime observation. To address this problem, Goita and Royer [36] extended the original TISI method to retrieve land surface emissivity from two consecutive data sets acquired at the same time during the daytime by simplifying the TISIE and the characteristics of the bidirectional reflectivity. However, their simplifications, particularly the case of  $TISIE = 1$ , will introduce some unexpected error into the retrieved emissivity and consequently the LST [30].

Inspired by the results in [35] and [38], a new daytime TISI method is proposed that uses the TISI method and the kernel-driven BRDF model to simultaneously retrieve emissivity and

temperature from a sufficient number of angular observations. First, the bidirectional reflectivity in the MIR channel can be expressed, on the basis of the kernel-driven BRDF model, as follows:

$$\rho_i(\theta_s, \theta_v, \varphi) = f_{iso} + f_{vol} \cdot k_{vol}(\theta_s, \theta_v, \varphi) + f_{geo} \cdot k_{geo}(\theta_s, \theta_v, \varphi) \quad (6)$$

where  $f_{iso}$  is the isotropic scattering term,  $f_{vol}$  is the coefficient of the volumetric kernel  $k_{vol}$ , and  $f_{geo}$  is the coefficient of the geometric kernel  $k_{geo}$ . The Ross-Thick volumetric kernel and the Li-SparseR geometric kernel are used in this paper. If the reflectivity  $\rho$  is known for at least three viewing directions, the three kernel coefficients ( $f_{iso}$ ,  $f_{vol}$ , and  $f_{geo}$ ) can be regressed using the least squares method. In contrast, if the three kernel coefficients are known in advance, the reflectivity  $\rho$  in arbitrary direction can be estimated from (6). Therefore, the retrieval of the reflectivity  $\rho$  will be equivalent to the retrieval of those kernel coefficients. Moreover, combining (4b) and (6) into (2) will produce a new formula

$$R_i(\theta_s, \theta_v, \varphi) = TISIE_{ij} \cdot R_j^{n_{ij}}(\theta_s, \theta_v, \varphi) \cdot M_{ij} \cdot C_{ij} + (f_{iso} + f_{vol} \cdot k_{vol} + f_{geo} \cdot k_{geo}) \cdot E_{sun}. \quad (7)$$

In (7), the terms  $R_i(\theta_s, \theta_v, \varphi)$  and  $R_j(\theta_s, \theta_v, \varphi)$  are the measured radiance in the MIR and TIR channels, respectively; the solar illumination  $E_{sun}$  can be estimated from atmospheric data [39];  $M_{ij}$  and  $n_{ij}$  are channel dependent and can be fitted using laboratory-simulated data; the index  $C_{ij}$  is complicated because it relies on both surface and atmospheric conditions and can be approximated as  $C_{ij} = [1 - R_{ai\downarrow}/B_i(T_{max})]/[1 - R_{ai\downarrow}/R_i]$ , where  $T_{max}$  is the maximum brightness temperature in the TIR channel under different viewing angles [35]. The rest of the terms of (7) are the unknown variables, including the three coefficients of the BRDF model and the TISIE. Although the emissivities of both MIR and TIR channels (i.e.,  $\varepsilon_i$  and  $\varepsilon_j$ ) vary with the viewing angle, the angular variation of the TISIE is not significant and is less than 0.01 for most cases. Therefore, it is reasonable to use only one average TISIE in (7) to reduce the number of unknowns. As a result, there are only four unknowns that remain (TISIE,  $f_{iso}$ ,  $f_{vol}$ , and  $f_{geo}$ ) in (7). If the same target is observed at more than four directions, those unknown  $X$  can be retrieved from the linear equation group, such as  $Y = AX$ , where  $A$  is the coefficient matrix composed by the terms in (7), and  $Y$  denotes  $R_i$ .

Once the three coefficients of the BRDF model are obtained, the directional emissivity in the MIR channel can be estimated as one minus the hemisphere-directional emissivity on the basis of Kirchhoff's law [38]. Hence

$$\varepsilon_i(\theta_v) = 1 - \rho_{hd} = 1 - \int_0^{2\pi} \int_0^{\frac{\pi}{2}} \rho(\theta_s, \theta_v, \varphi) \sin(\theta_s) \cos(\theta_s) d\theta_s d\varphi. \quad (8)$$

According to (6), the integration of the reflectivity in the upward hemisphere is equal to the result of integrating the three kernels ( $k_{vol}$ ,  $k_{geo}$ , and 1) in the same angle range because the values of the kernel coefficients are fixed for all angles.

Jiang *et al.* [38] calculated the integration of the Ross-Thick volumetric kernel ( $I_{k_{vol}}$ ) and Li-SparseR geometric kernel ( $I_{k_{geo}}$ ) with SZA varying from  $0^\circ$  to  $80^\circ$  and SAA varying from  $0^\circ$  to  $360^\circ$  with a step  $0.05^\circ$  and then related  $I_{k_{vol}}$  and  $I_{k_{geo}}$  to the VZA ( $\theta_v$ ) using an exponent growth function and a Gaussian function, respectively. Finally, based on the concept of the two-channel TISIE defined in (4), the emissivity in the TIR channels can be obtained from the TISIE and the emissivity in the MIR channel as (9) [34], [35], and consequently, the surface temperature at the current viewing direction can be calculated from the inversion of the thermal radiative transfer equation

$$\varepsilon_j(\theta_v) = \left( \frac{\varepsilon_i(\theta_v)}{\text{TISIE}_{ij}} \right)^{1/n_{ij}}. \quad (9)$$

The advantage of the above daytime TISI method (hereafter called the D-TISI method) is that it eliminates the requirement of daytime and nighttime measurements in the original TISI method by using at least four angular observations in both MIR and TIR channels, and it requires only one atmospheric correction for all angular observations instead of two, respectively, for the daytime and nighttime observations. However, because the temperature difference between those angular observations is not as large as that of the daytime and nighttime observations, the relatively high correlations in the radiative transfer equations like (7) may make the method sensitive to data error. Therefore, an optimization algorithm is needed to avoid outliers, and this paper used the constrained linear least-squares optimization algorithm included in the function *lsqlin()* of the MATLAB software.

It is worth noting that all variables/parameters in the above equations, except for the angles, are channel-effective values. The channel-effective quantities of interest are calculated as a weighted value from monochromatic values using the spectral response function  $f(\lambda)$ : [30]

$$X_i = \frac{\int_{\lambda_1}^{\lambda_2} f_i(\lambda) X_\lambda d\lambda}{\int_{\lambda_1}^{\lambda_2} f_i(\lambda) d\lambda} \quad (10)$$

where,  $\lambda_1$  and  $\lambda_2$  are the lower and upper response wavelength of the  $i$ th channel, respectively, and  $X$  stands for  $B(T)$ ,  $R$ ,  $L$ ,  $R_{a\downarrow}$ ,  $R_{a\uparrow}$ ,  $R_{sl\uparrow}$ ,  $\varepsilon$ ,  $\tau$ , or  $\rho$ . Equations (1) and (2) are actually approximations of the theoretical radiative transfer equation in which monochromatic quantities are replaced with channel-effective values, and those approximations are only reliable for a narrow channel.

### III. MODEL ANALYSIS

#### A. Channel Specifications

We were concerned with the MIR and TIR channels from two sensors: the airborne WiDAS system [27], [40] used in the WATER field campaign [29] and the MODIS channels 20 and 31. The MIR and TIR images of the WiDAS will be used in the next section for the validation of the D-TISI method. However, as shown in Fig. 1, the bandwidths of the WiDAS's two channels are up to 4 and 11  $\mu\text{m}$ , respectively, which are rare in current airborne or spaceborne sensors and will reduce

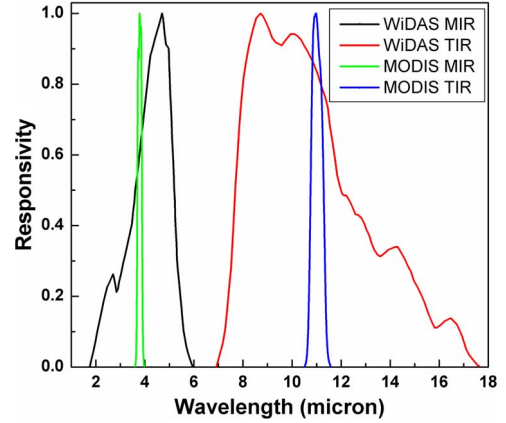


Fig. 1. Spectral response function of the MIR and TIR channels for the WiDAS system and the MODIS sensor, respectively.

the accuracy of the approximations of the radiative transfer function from the monochromatic value to the channel-effective value as stated in (10), in addition to degrading the accuracy of the approximation of the exponent expression of the channel radiance using (3). In contrast, the bandwidths of the MODIS's MIR and TIR channels are relatively narrower, and such narrow bandwidths are usually observed for several sensors. Therefore, although this paper will not use the MODIS data to validate the D-TISI method due to the lack of multiangular observation images, the following analysis will discuss the retrieved results from the MODIS's two channels in detail rather than the WiDAS system, to make the findings of this paper more representative and reliable, and only provide the general results for the WiDAS system.

Table I shows the coefficients  $m$  and  $n$  in (3) for the channels of MODIS and WiDAS. Two temperature ranges, i.e., 270–300 K and 300–330 K, were used for the exponent approximation with higher accuracy. In the retrieval process,  $m$  and  $n$  can be determined with the measured TIR brightness temperature.

#### B. Simulation Conditions

Many surface and atmospheric conditions have to be designed to simulate the bidirectional reflectivity in the MIR and the directional emissivity and measured radiance of the MIR and TIR channels. Because the D-TISI method needs the surface-leaving radiance after atmospheric correction, we only considered the middle-latitude summer atmospheric models included in the MODERate resolution atmospheric TRANsmission (MODTRAN) V4.0 radiative transfer code. The rural aerosol model was assumed with a visibility of 10, 15, 20, 25, 30, 40, and 50 km, and the column water vapor was set with 0.25, 0.5, and 0.75  $\text{WV}_{\text{max}}$ , where  $\text{WV}_{\text{max}}$  is the maximum water content in the atmospheric model.

The Scattering by Arbitrarily Inclined Leaves (SAIL) Hotspot (SAILH) model [41] was used to simulate the bidirectional reflectivity in the MIR channel and the directional emissivities in both MIR and TIR channels. The SAILH model was inherited from the scattering by SAIL model [42], which incorporated the foliage hotspot effect according to the theory of Kuusk [43], and the results of the SAILH model should be closer to reality than the original model. The input variables

TABLE I  
PARAMETERS  $m$ ,  $n$ , AND ERROR (RMS AND MAX) FOR THE MIR AND TIR CHANNELS OF MODIS AND WiDAS

Sensor&Channel	270 K ~ 300 K				300K ~ 340 K				
	$Ln(m)$	$n$	$\Delta L(rms)$	$\Delta L(max)$	$Ln(m)$	$n$	$\Delta L(rms)$	$\Delta L(max)$	
MODIS	MIR	-76.68	13.32	0.002	0.006	-68.43	11.87	0.009	0.032
	TIR	-24.18	4.64	0.014	0.036	-21.46	4.16	0.029	0.078
WiDAS	MIR	-60.57	10.67	0.003	0.011	-54.74	9.65	0.014	0.047
	TIR	-26.01	4.95	0.012	0.032	-23.49	4.51	0.027	0.073

of the SAILH model include the canopy parameters (e.g., leaf area index (LAI) and hotspot factor) and component properties (e.g., reflectivity and transmittance). The SAILH model outputs the bidirectional reflectivity at any designed viewing geometry. Furthermore, the hemisphere-directional reflectivity of the canopy is integrated from the bidirectional reflectivity in the hemisphere, and the directional emissivity is estimated as the complement of the hemisphere-directional reflectivity based on Kirchhoff's law. Although this paper concerns nonisothermal surfaces, the emissivity is assumed to be independent of the temperature distribution of the surface [44]. As a result, Kirchhoff's law is still suitable at least for the aforementioned calculation of the directional emissivity over the nonisothermal surface.

We chose ten vegetation samples and 17 soil samples from the University of California at Santa Barbara (UCSB) spectral emissivity databases and obtained their channel emissivity for the MIR and TIR channels using (10), which resulted in a total of 170 combinations of vegetation and soil samples. Table II shows the channel emissivity of the MODIS and WiDAS. Because the wavelength range (3–14  $\mu\text{m}$ ) of the sample emissivities did not cover all the response wavelengths of the WiDAS's two channels, the spectral emissivity out of the 3–14  $\mu\text{m}$  was not used in the integration procedure from monochromatic emissivity to the channel emissivity. Note that sample emissivities were assumed to be angle independent. Furthermore, those samples' reflectivity input to the SAILH model was calculated as the complement of the channel emissivity listed in Table II, and the transmittance of the samples was equal to zero. A spherical canopy was assumed in the SAILH model, and the LAI varied from 0.5 to 5 with a step of 0.5.

As shown in Fig. 2, the simulated TISIE in the MODIS channels mainly distributes in the range [0.95, 1.1], whereas some TISIE values are smaller than 0.9 because of the low emissivity of some soil samples in the MIR channel and the small LAIs. According to the results obtained by Jiang *et al.* [35], the pixel TISIE values were mostly larger than 0.96 for several different combinations of the MIR and TIR channels. Therefore, in order to make the simulated TISIE close to the reality and also to ensure the retrieval result to be more representative, we consider the case of TISIE larger than 0.92, which covers approximately 92% of the total samples and most of the natural surface.

The nonisothermal canopy was assumed to consist of three components: leaves, sunlit soil, and shaded soil. Six groups of those three components' temperatures were used, as shown

TABLE II  
CHANNEL EMISSIVITY FOR THE MODIS AND WiDAS SYSTEM,  
CHOSEN FROM UCSB EMISSIVITY DATABASE

MODIS	MODIS	WiDAS	WiDAS	Sample Name
MIR	TIR	MIR	TIR	
Vegetation Samples				
0.9566	0.9626	0.9572	0.9572	Leaf of Maple
0.9384	0.9535	0.9096	0.9664	Dry Grass (Averaged over 9 Sets)
0.9392	0.9540	0.9103	0.9669	Dry Grass3 (Averaged over 9 Sets)
0.9691	0.9601	0.9677	0.9617	Fresh leaf of Eucalyptus tree
0.9724	0.9714	0.9714	0.9742	Laurel leaf
0.9586	0.9563	0.9577	0.9525	Leaf Magnolia
0.9642	0.9617	0.9638	0.9621	Leaf of Evergreen Pear
0.9856	0.9908	0.9860	0.9914	Leaf of Green Spruce from Canada
0.9841	0.9807	0.9844	0.9809	Leaf of Pine (New)
0.9781	0.9792	0.9786	0.9787	Leaf of Pine (Old)
Soil Samples				
0.9248	0.9681	0.9369	0.9618	Salty Soil (Averaged over 19 Sets)
0.8392	0.9581	0.9242	0.9012	Sand Sample 2 from Orchard
0.8467	0.9719	0.8694	0.9571	No.88p2535S from Nebraska Soil Lab
0.6816	0.9590	0.7503	0.9531	No.88p3715S from Nebraska Soil Lab
0.8252	0.9789	0.8597	0.9656	No.88p4643S from Nebraska Soil Lab
0.6066	0.9477	0.6869	0.9380	No.90p3101S from Nebraska Soil Lab
0.6918	0.9712	0.7519	0.9532	No.90P4172S from Nebraska Soil Lab
0.7793	0.9746	0.8347	0.9586	No.90P4255S from Nebraska Soil Lab
0.8501	0.9760	0.8885	0.9656	Soil Sample 1 from Concord, MA
0.7858	0.9828	0.8408	0.9535	Soil Sample 10 from Oklahoma
0.7842	0.9767	0.8431	0.9497	Soil Sample 13 from Oklahoma
0.8712	0.9744	0.8938	0.9631	Soil Sample 3 from Concord, MA
0.8493	0.9673	0.9077	0.9568	Soil Sample 4 from Death Valley, CA
0.8548	0.9758	0.9047	0.9512	Soil Sample 5 from Oklahoma
0.8346	0.9679	0.8700	0.9438	Soil Sample 7 - Hard Pan
0.7569	0.9661	0.8602	0.9301	Soil Sample 7 from Death Valley, CA
0.8418	0.9725	0.8905	0.9449	Soil Sample 9 - Hard Pan, Ground

in Table III. T-groups 1 and 2 represent low components' temperatures with small and large differences, respectively. T-groups 3 and 4 represent middle temperatures with small and large differences, respectively. Finally, T-groups 5 and 6 represent high temperatures, and their temperature differences

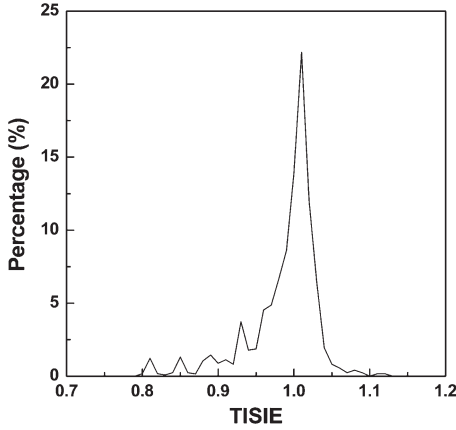


Fig. 2. Histogram of TISIE in the MODIS simulated data set.

TABLE III  
DIFFERENT GROUPS OF COMPONENTS' TEMPERATURES  
USED FOR SIMULATIONS

T-group No.	$T_{leaf}$ (K)	$T_{sun\_soil}$ (K)	$T_{shd\_soil}$ (K)
1	270	280	273
2	270	285	275
3	290	300	293
4	290	305	295
5	310	325	315
6	310	330	320

are generally larger than the other groups because both cases may occur in sparse canopies and/or in summer.

### C. Canopy Directional Radiance and Directional Effective Temperature

Based on the simulation conditions aforementioned, the bidirectional reflectivity and emissivity were simulated with the SAILH model, and the downward atmospheric radiance and solar radiance in (2) were determined from MODTRAN4.0. The canopy directional effective radiance in (2) (i.e.,  $L_e(\theta_s, \theta_v, \varphi) = \varepsilon(\theta_v)B[T(\theta_s, \theta_v, \varphi)]$ ) was further simulated as follows:

$$L_e(\theta_s, \theta_v, \varphi) = \sum_{k=1}^3 f_k(\theta_s, \theta_v, \varphi) \cdot L_k + L_{\text{multi}} \quad (11)$$

$$L_{\text{multi}} = \sigma_f L_{\text{leaf}} (1 - \varepsilon_s) b(\theta) + (1 - \alpha) [1 - b(\theta)(1 - \sigma_f)] \cdot [1 - b(\theta)] (1 - \varepsilon_v) \cdot L_{\text{leaf}}. \quad (12)$$

The first term of (11) is the weighted radiance by the component fraction  $f_k$ , which is calculated from a parameterization model of the SAILH model in [45], at the viewing geometry  $(\theta_s, \theta_v, \varphi)$ , and the component emitted radiance  $L_k$  calculated from the emissivity (see Table I) and temperature (see Table II) using Planck's law. The second term of (11) is the radiance scattering between the leaves and the soil [see the first part of the right-hand side of (12)] and between leaves [see the second part of the right-hand side of (12)] in the canopy.  $b(\theta)$  is the directional gap of the canopy, and  $\sigma_f$  is the hemispheric leaf fraction; both of them can be determined by using canopy LAI

TABLE IV  
DIFFERENT ANGLE COMBINATIONS

Case No.	Angle combination (VAA, VZA)	Description
1	$(0^\circ, 0^\circ); (0^\circ, 10^\circ), (0^\circ, 30^\circ)$ and $(180^\circ, 10^\circ), (180^\circ, 30^\circ)$	five angles: nadir, forward and backward $10^\circ$ and $30^\circ$
2	$(0^\circ, 0^\circ); (0^\circ, 30^\circ), (0^\circ, 50^\circ)$ and $(180^\circ, 30^\circ), (180^\circ, 50^\circ)$	five angles: nadir, forward and backward $30^\circ$ and $50^\circ$
3	$(0^\circ, 0^\circ); (0^\circ, 20^\circ), (0^\circ, 40^\circ)$ and $(180^\circ, 20^\circ), (180^\circ, 40^\circ)$	five angles: nadir, forward and backward $20^\circ$ and $40^\circ$
4	$(0^\circ, 0^\circ); (0^\circ, 10^\circ), (0^\circ, 20^\circ), (0^\circ, 40^\circ);$ and $(180^\circ, 0^\circ), (180^\circ, 20^\circ), (180^\circ, 40^\circ)$	seven angles: nadir, forward and backward $10^\circ, 20^\circ$ and $40^\circ$

and viewing angles.  $\alpha$  denotes the cavity effect accounting for the multiple scattering inside the canopy. More details about the calculation of  $b(\theta)$ ,  $\sigma_f$ , and  $\alpha$  can be found in [32]. On the basis of the  $L_e(\theta_s, \theta_v, \varphi)$  simulated from (11), we defined the directional brightness temperature (DBT) and the directional effective temperature ( $T_e$ ) for the nonisothermal canopy as (13).  $B[]^{-1}$  is the inversion of Planck's law. Note that the consideration of the nonisothermal canopy causes  $T_e$  to vary with channels, which does not satisfy the requirement of the D-TISI method that the temperature must be the same in the MIR and TIR channels. To satisfy the requirement, the  $T_e$  of the MIR channel was forced to equal that of the TIR channel in our simulated data set. However, the DBTs were channel dependent. Hence

$$\text{DBT}(\theta_s, \theta_v, \varphi) = B [R(\theta_s, \theta_v, \varphi)]^{-1} \\ T_e(\theta_s, \theta_v, \varphi) = B \left[ \frac{L_e(\theta_s, \theta_v, \varphi)}{\varepsilon(\theta_v)} \right]^{-1}. \quad (13)$$

### D. Multiple Angular Combinations

As previously stated, at least four angular observations are required to solve the four unknowns. A previous study indicated that a large difference among VZAs can reduce the correlations between radiative transfer equations and can obtain more accurate results in the retrieval of emissivity and temperature [31]. To illustrate the influence of the different angular observations on the retrieval accuracy, we used four groups of angular observations (see Table IV). The fourth group is the designed angular combination of the WiDAS system. In addition, we assumed that the backward direction has a VAA of  $180^\circ$ , and the forward direction has an azimuth angle of  $0^\circ$ .

### E. Initial Values of the Four Unknowns

The initial value of the TISIE can be obtained using a similar relationship between the TISIE and the ratio of the MIR and

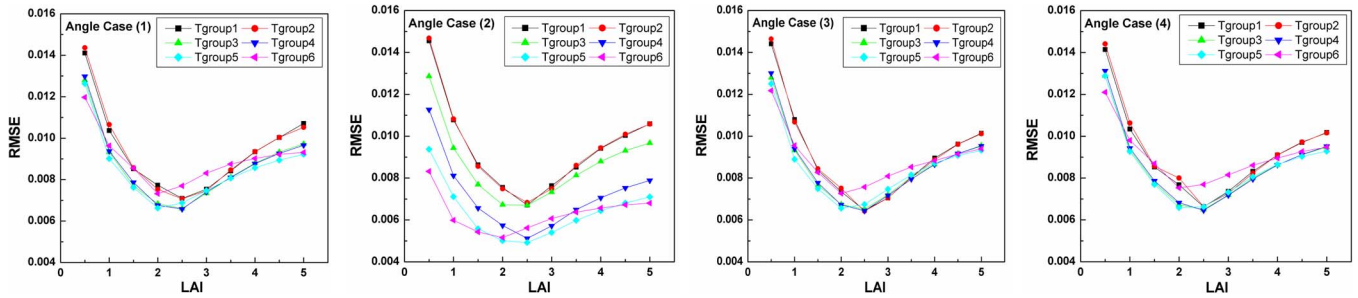


Fig. 3. RMSE of TIR emissivity at different angular observations and LAIs, with DBT noise of the MIR and TIR channels within  $[-0.5, 0.5]$  K included in the directional brightness temperature of both MIR and TIR channels. The components' temperatures of each T-group are shown in Table III.

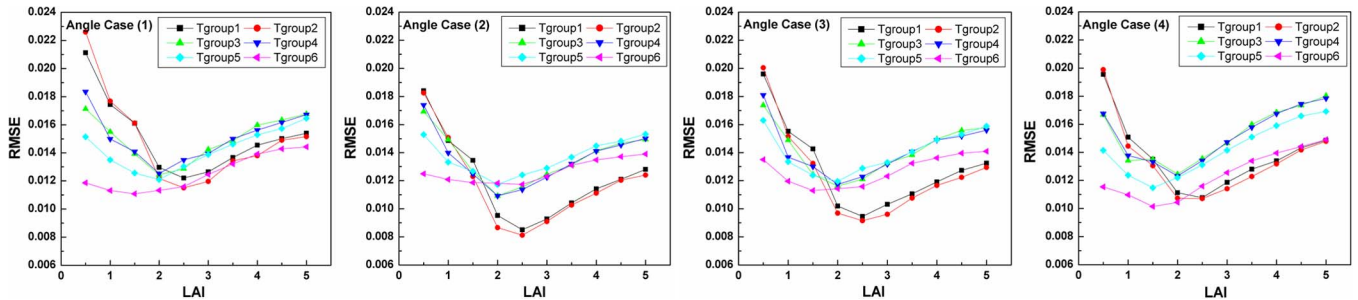


Fig. 4. Similar to Fig. 3 but with DBT noise within  $\pm[0.5, 1.0]$  K.

TIR surface-leaving radiance, as proposed in [36]. With the known atmospheric downward radiance from atmospheric data, we first used  $\varepsilon_j = 0.98$  ( $j$  denotes the TIR channel) to retrieve the  $T_e$  in the TIR channel and applied  $T_e$  in the radiative transfer equation [i.e., (2)] to calculate the bidirectional reflectivity with an approximation  $\rho(\theta_s, \theta_v, \varphi) = 1 - \varepsilon(\theta_v)$ , and then, we estimated the three coefficients ( $f_{iso}$ ,  $f_{vol}$ , and  $f_{geo}$ ) from the BRDF model shown in (6). These initial values were consequently input into the optimization algorithm to obtain the final solution of the four unknowns.

*F. Model Analysis*

Because the observed data always included some noise from the instrument noise, atmospheric correction, and angle-controlling error, the retrieval accuracy may be consequently degraded. To evaluate the model's consistency with the LAI and angular combination, as well as temperature and TISIE themselves, some artificial noise was introduced into those data. The noise included in the atmospheric data ranged from  $[-10\%, 10\%]$  of the data itself, and the noise introduced in the DBT of the MIR and TIR channels was within  $[-0.5, 0.5]$  K and  $\pm[0.5, 1.0]$  K. The two types of DBT noise were used to investigate the reliability of the four aforementioned angular combinations. All noise was provided with a uniform distribution. Note that the results shown in Figs. 3–7 are from the MIR and TIR channels of the MODIS sensor, whereas the results in Fig. 8 are for the WiDAS system.

1) *Influence of LAI*: In Figs. 3 and 4, The root-mean-square error (RMSE) of the retrieved TIR emissivity is displayed for the equivalent temperature noise within  $[-0.5, 0.5]$  K, which is included in the simulated DBT, and for the noise within  $\pm[0.5, 1.0]$  K, respectively. As observed in the two figures, the RMSE initially decreases and then increases with the in-

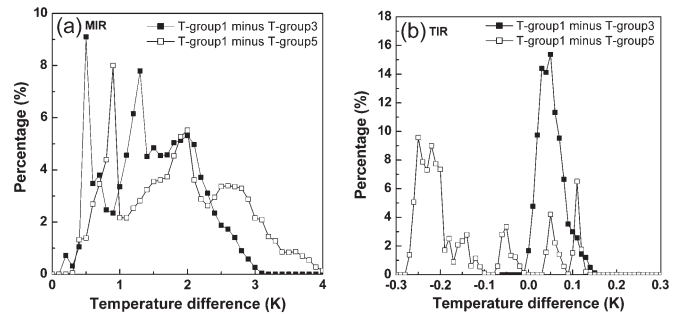


Fig. 5. Histograms for the difference of the temperature discrepancy between nadir and off-nadir  $50^\circ$  observations in (a) MIR and (b) TIR channels of T-group 1 against T-groups 3 and 5, respectively.

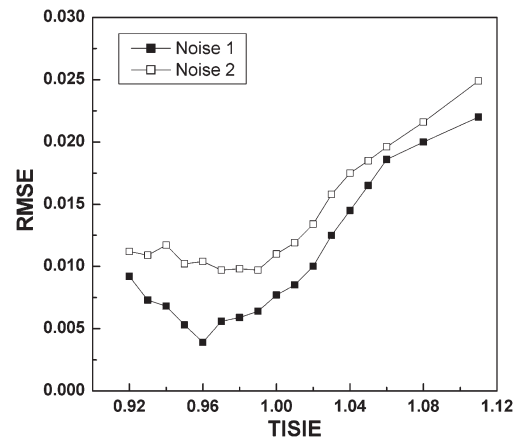


Fig. 6. Influence of TISIE on the retrieval accuracy by using angle case 2.

creasing LAIs. As for the sparse (e.g., LAI = 0.5) or dense (e.g., LAI > 4) vegetated surfaces, their angular variations of the components' fractions and DBT were not remarkable, and consequently, the solution of (7) was sensitive to the noise

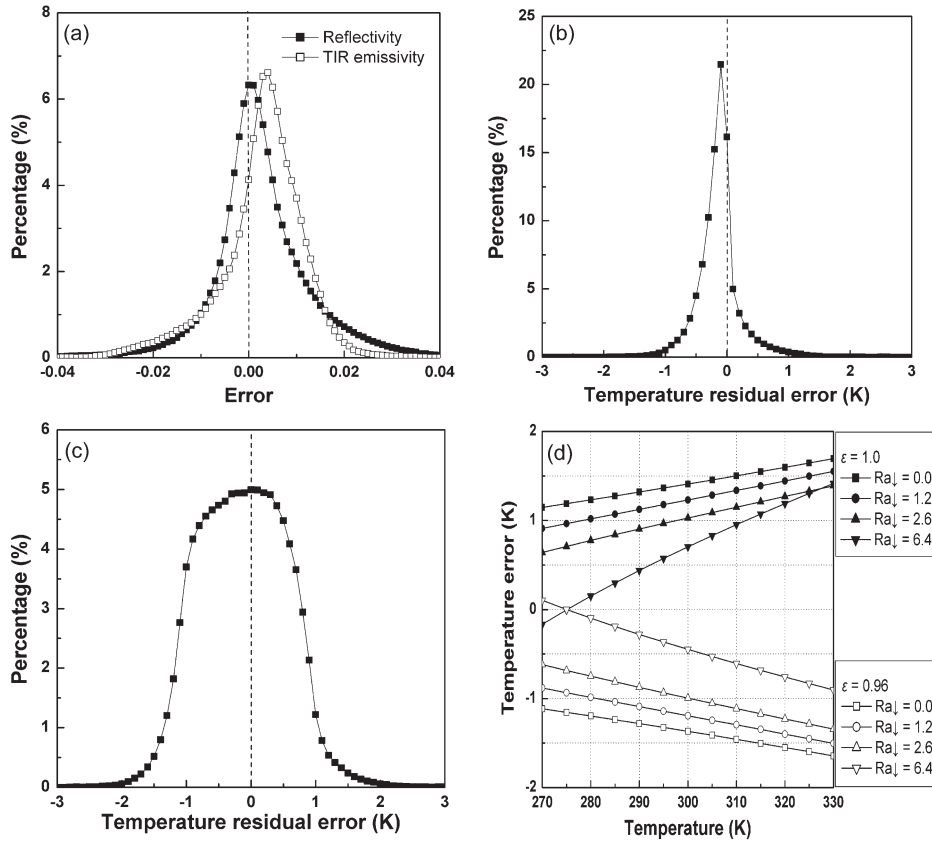


Fig. 7. (a) Histograms of the retrieval error for the bidirectional reflectivity in the MIR channel and emissivity in the TIR channel at DBT noise within  $[-1.0, 1.0]$  K. (b) Histogram of the residual error of the directional effective temperature  $T_e$  calculated from the retrieved TIR emissivity and the directional radiance and atmospheric data without noise. (c) Histogram of the residual error of  $T_e$  calculated from the retrieved TIR emissivity and the directional radiance and atmospheric data with noise. (d) Theoretical temperature error caused by emissivity error ( $\pm 0.02$  at true  $\epsilon = 0.98$ ) under different temperatures and downward atmospheric radiances (unit:  $W/m^2/sr/\mu m$ ). Angle case 2 was used for illustration.

included in the MIR and TIR brightness temperatures and atmospheric data. In contrast, for the partly vegetated surface (e.g., LAI = 1.5 and 2.0), the variation of the components' fractions and DBT caused by different viewing angles becomes relatively more significant, whereas the retrieval process is less influenced by the noise in the input data.

2) *Influence of Angular Combinations*: As previously stated, four groups of angular observations were used to determine the “best” combination for the retrieval of the bidirectional reflectance and emissivity. The retrieval RMSE for most cases in Fig. 3 is smaller than 0.01, and all of them are less than 0.015, whereas for most cases in Fig. 4, the RMSEs are less than 0.015. The greater noise included in the DBT produced larger error in the retrieved emissivity. A comparison between the results from different cases of the angular combinations indicates that case 2 performs better than the others, particularly for the DBT noise within  $[-0.5, 0.5]$  K, most likely because case 2 had the largest off-nadir observation (i.e., VZA =  $50^\circ$ ) and the largest angle interval (i.e.,  $\Delta VZA = 30^\circ$  or  $20^\circ$ ) (see Table IV), which corresponded to the largest difference in the components' fractions and DBT between the different viewing angles and consequently reduced the correlation of the radiative transfer equations, resulting in a more reliable retrieval result. On the other hand, the smallest off-nadir observation (i.e., VZA =  $50^\circ$ ) and angle interval (i.e.,  $\Delta VZA = 10^\circ$  or  $20^\circ$ ) in case 1 enhanced the correlations of their radiative transfer

equations, leading to the lowest retrieval accuracy. Comparing the results of cases 3 and 4, case 3 performed slightly better than case 4, particularly for T-groups 1 and 2. This better performance might be due to the fact that, although case 4 has more angular observations (seven) than case 3, the correlations of the radiative transfer equations were increased by the smaller angle interval in case 4, and the error included in the additional angular observation can also degrade the retrieval accuracy. Therefore, more observations will not always obtain more accurate results unless the angle interval is large enough.

From the aforementioned discussion and the results shown in Figs. 3 and 4, we determined that case 2 is the best angular combination among the four examined angle cases, and these results are similar to a previous study [31]. However, these results do not mean that case 2 involves the best angular combinations for the retrieval, since it is actually difficult to determine the best combination from numerous combinations with different viewing angles in the upper hemisphere. Although a large viewing angle can improve the retrieval accuracy, it is not recommended to use a viewing angle larger than  $55^\circ$  because the pixel size of such viewing angle is approximately four times the size of the nadir observation, and the different pixel sizes may result in the presentation of different components and/or their temperatures, particularly for heterogeneous surfaces.

3) *Influence of Components' Temperatures*: The correlation between the radiative transfer equations of different viewing



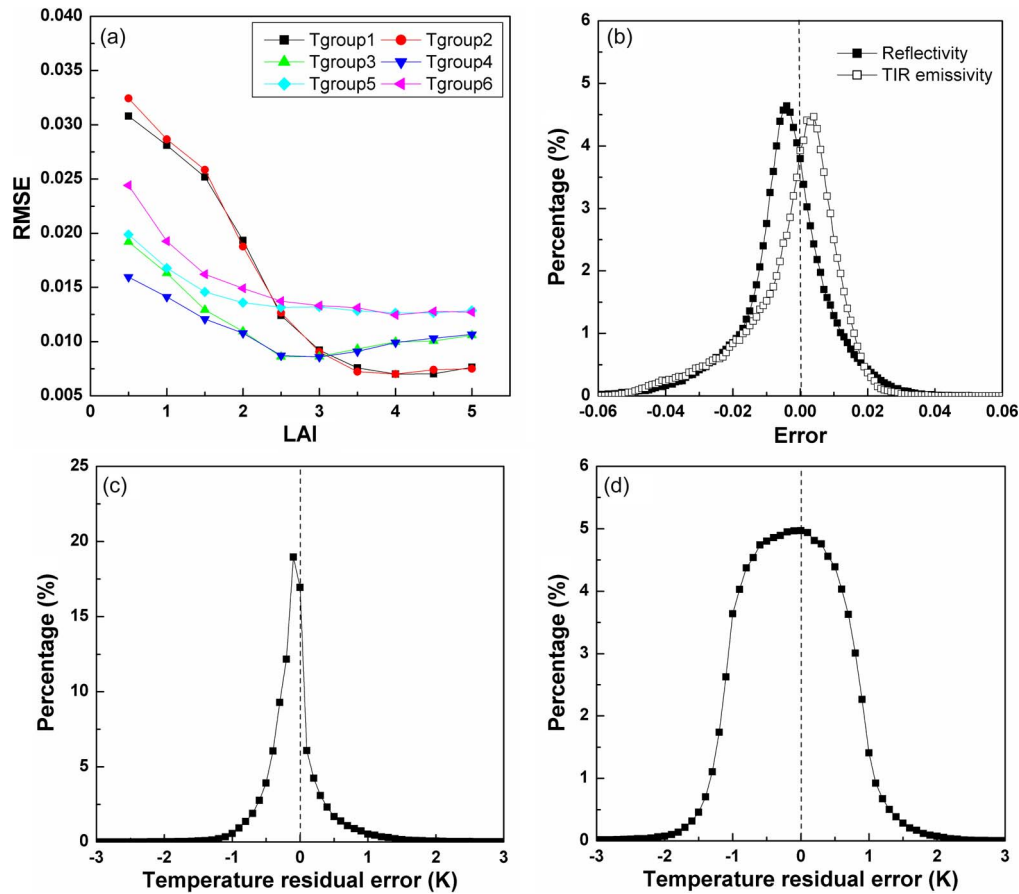


Fig. 8. (a) RMSE of TIR emissivity at different LAIs and components' temperatures for the WiDAS system. (b) Histograms of the retrieval error for bidirectional reflectivity in the MIR channel and emissivity in the TIR channel for the WiDAS system. (c) Histogram of the residual error of directional effective temperature  $T_e$  calculated from the retrieved TIR emissivity and the directional radiance and atmospheric data without noise. (d) Histogram of the residual error of  $T_e$  calculated from the retrieved TIR emissivity and the directional radiance and atmospheric data with noise. Angle case 4 was used for illustration.

angles is related to the temperature discrepancy of the components in the scene. Large temperature discrepancies can reduce this correlation, whereas small temperature discrepancies can lead to a higher correlation. As shown in Table III, T-groups 1 and 2 had a similar level of different components' temperatures, but the temperature discrepancy for T-group 2 was larger than that for T-group 1. Therefore, since the correlation of the angular observation is less significant in T-group 2, the retrieval error of T-group 2 is smaller than T-group 1, as shown in Figs. 3 and 4. A similar case was found for T-groups 3 and 4 and T-groups 5 and 6. However, this difference of the retrieval errors between T-groups 1 and 2, T-groups 3 and 4, and T-groups 5 and 6 was so limited that it almost disappeared in some results, as observed in Fig. 3, perhaps because the relatively smaller temperature difference in T-groups 1, 3, and 5 is large enough to reduce the influence of the temperature difference and also because of the influence of noise included in the measured data.

Fig. 4 also shows that the retrieval errors of T-groups 1 and 2 were almost smaller than those of the other T-groups with higher DBT, particularly for the angle cases 2 and 3. These results indicate that the increase in DBT could not enable a better retrieval result, due to the fact that, at the same level of the difference of the components' temperatures, the increase in components' temperatures inversely reduced the angular variation of the DBT between the angular observations. Fig. 5

presents the histograms of the difference  $\Delta T' = \Delta T_1 - \Delta T_x$  of temperature contrast between the nadir and off-nadir  $50^\circ$  observations, where  $\Delta T_1 = T_{\text{nadir}} - T_{50^\circ}$  in T-group 1 and  $\Delta T_x = T_{\text{nadir}} - T_{50^\circ}$  ( $x = 3$  and  $5$ ) in T-groups 3 and 5. It was observed that the temperature contrast between the nadir and off-nadir  $50^\circ$  observations in T-group 1 was larger than that of T-groups 3 and 5, particularly for the MIR channel. As for T-groups 1 and 3 (see filled squares in Fig. 5(a) and (b)), the temperature contrast  $\Delta T_1$  was notably larger than  $\Delta T_3$  for both the MIR and TIR channels, and all of the  $\Delta T'$  values in the TIR channel ranged from 0.0 to 0.2 K, whereas most of the  $\Delta T'$  values in the MIR channel were more than 1.0 K. Consequently, this variation in the temperature contrast of nadir and off-nadir directions, from a lower temperature (such as T-group 1) to a higher temperature (such as T-group 3) but with similar difference of components' temperatures, caused a corresponding higher correlation in radiative transfer equations and finally made the retrieval process from T-group 3 to be more sensitive to the noise than that from T-group 1. As for T-groups 1 and 5 [see unfilled squares in Fig. 5(a) and (b)], the  $\Delta T'$  between  $\Delta T_1$  and  $\Delta T_5$  of the MIR channel was notable and generally larger than the  $\Delta T'$  between  $\Delta T_1$  and  $\Delta T_3$ . However, as shown in Fig. 5(b), most of the  $\Delta T_1$  were smaller than  $\Delta T_5$ , which means that the temperature contrast between the nadir and off-nadir  $50^\circ$  observations was enlarged in the TIR channel

from T-group 1 to T-group 5. As a result, this variation might cause T-group 5 to obtain a more accurate result than T-group 3 in theory. However, due to the fact temperature contrast in the MIR channel was remarkably reduced, the retrieval accuracies from T-group 5 were generally lower than that from T-group 1 and even lower than that from T-group 3 in some cases. Similar reasons can be used to explain the variation between T-groups 2 and 4. T-group 6 had a better result because its components' temperature contrast was larger than the other groups. From the aforementioned discussions, a cautious conclusion can be drawn that, at the same level of components' temperature differences, the case with a relatively lower brightness temperature will lead to better results for the retrieval emissivity in the TIR channel, as well as for the bidirectional reflectivity and emissivity in the MIR channel. However, the results still depend on the specific situation, including the atmospheric conditions and canopy structures.

4) *Influence of TISIE*: Fig. 6 presents the RMSE for the retrieved TIR emissivity, which varies with the TISIE for two noise conditions. Only angle case 2 was used for illustration. These data show that the RMSEs for the TISIE within [0.92, 1.06] were smaller than 0.015, which is the accuracy required for some sensors [9]. According to the histogram in Fig. 2, this part of the TISIE covers approximately 92% of all samples and approximately 98% of the samples with a TISIE larger than 0.92. Moreover, this range of TISIE also covers the values of most natural surfaces, as reported by Jiang *et al.* [35], on satellite data. However, for those larger TISIEs (i.e., > 1.05) resulting from dense vegetated surfaces or sparse surfaces (or dry grass and mafic surfaces, e.g., volcanics, in natural surface) whose MIR emissivity is relatively larger and TIR emissivity is relatively smaller, the retrieval accuracy might be degraded by the small angular variation of the components' fractions and DBT, as described earlier.

Based on the aforementioned simulated data set, Fig. 7(a) displays the histograms of the residual error for the retrieved bidirectional reflectivity in the MIR channel and emissivity in the TIR channel with DBT noise within [-1.0, 1.0] K. These results show that the bias of reflectivity was close to 0, but that of the TIR emissivity was larger than 0 and nearly 0.004, which indicates that the retrieved TIR emissivity was generally larger than the true value and that the accuracy of the retrieved reflectivity was higher than that of the TIR emissivity. This result is reasonable due to the fact that, from (7) and the kernel-driven BRDF model in (6), the accuracy of the bidirectional reflectivity is only influenced by the three coefficients driven from (7), whereas that of the TIR emissivity is not only dependent on the three coefficients but also relies on TISIE. Since the error of the parameter  $C_{ij}$  described in (4) can degrade the accuracy of the TISIE solution, the errors of TISIE and the MIR emissivity calculated from the BRDF model using the retrieved three coefficients can be further enlarged by the exponential conversion of (9).

Fig. 7(b) and (c) shows the histograms of the residual error for the directional effective temperature  $T_e$  [see (13)] calculated from the inversion of the radiative transfer equation using the retrieved TIR emissivity with true DBT and downward atmospheric radiance, and with the noise-added DBT and downward

atmospheric radiance, respectively. Therefore, Fig. 7(b) can be considered as the DBT residual error only caused by the error of the TIR emissivity, whereas Fig. 7(c) can be considered as the residual error caused by the error of the TIR emissivity and the noise included in the DBT itself and the atmospheric radiance. As observed in Fig. 7(b), the DBT residual error mainly (96%) fell into a range of [-1.0, 1.0] K, and the temperature residual with the maximum percentage of the histogram was close to 0. To investigate the results in Fig. 7(c), Fig. 7(d) presents the theoretical temperature error caused by emissivity error ( $\pm 0.02$  at true  $\varepsilon = 0.98$ ) under different true temperatures and downward atmospheric radiances. The temperature error in this figure was calculated as the difference of the true temperature minus the retrieved temperature from the inversion of Planck's law with given emissivity (0.96 or 1.0). Results shown in Fig. 7(d) indicate that the absolute temperature error increased with the increasing temperature itself, but decreased with the increasing downward atmospheric radiance, because emissivity error has less influence on the reflected downward atmospheric radiance. It is possible for an emissivity error of 0.02 to lead to a temperature error within [-1.0, 1.0] K, particularly for low temperatures and/or large downward atmospheric radiance. Therefore, the results shown in Fig. 7(b) are reasonable. Compared with Fig. 7(b), the actual range of the DBT residual error in Fig. 7(c) was relatively larger, and the residual error within [-0.8, 0.5] K is at a similar percentage because of the influence of the noise included in the DBT itself and the atmospheric radiance. However, Fig. 7 still demonstrates that the bidirectional reflectivity and emissivity can be retrieved within an error lower than 0.015, and the DBT can be obtained with an error within 1.5 K for most cases from multiangular observations using the angle combination of case 2.

The aforementioned model analysis was concerned with the MIR and TIR channels of the MODIS sensor because this sensor has narrower bandwidth than the WiDAS system and is more representative of most current sensors. However, it is necessary to illustrate the result for the WiDAS system because its MIR and TIR data will be used to validate the D-TISI method. Fig. 8(a) displays the RMSE variation of the TIR emissivity, which is retrieved from the DBT at noise within [-1.0, 1.0] K and downward atmospheric radiance at noise within [-10%, 10%], with the canopy LAIs and components' temperature combinations. The angle case 4 was used because this angle case was designed for the WiDAS system. Compared with Figs. 3(d) and 4(d), the RMSE for the WiDAS system is similar to that of the MODIS, except for the RMSE (up to 0.035) in the lower LAIs of T-group 1 and T-group 2.

Fig. 8(b) is the corresponding histogram of the residual error of the MIR bidirectional reflectivity and TIR emissivity for the WiDAS system, which indicates that their residual error was distributed widely from -0.06 to 0.06 and that there was a bias of approximately -0.004 and 0.004 for the reflectivity and emissivity, respectively. A comparison between Figs. 7(a) and 8(b) highlights that the retrieval accuracy of the WiDAS system was generally lower than that of the MODIS, most likely due to its broader bandwidths in both the MIR and TIR channels. According to the simulated DBT of the MODIS and WiDAS system using (11) and (12), we observed that

TABLE V  
SPECIFICATION OF THE WiDAS SYSTEM

	CCD camera	MIR camera	TIR camera
Spectral channel	550nm, 650nm,700nm and 750nm(with band width 40nm)	Mainly in 3~5 $\mu$ m	Mainly in 8~12 $\mu$ m
Pixels	1392 $\times$ 1040	320 $\times$ 240	
Total FOV	60 $^\circ$	80 $^\circ$	
I FOV	0.8 $\mu$ rad	4.24 $\mu$ rad	
Nadir resolution	1.25m@1.5km	7.9m@1.5km	
View zenith	Five angles between forward 30 $^\circ$ and backward 30 $^\circ$	Seven angles between forward 40 $^\circ$ and backward 40 $^\circ$	

the broader bandwidth degraded the retrieved accuracy of the reflectivity and emissivity in two different ways: first, because some response wavelengths of the MIR channel were out of the atmospheric window of 3–5  $\mu$ m, as shown in Fig. 1, the transmittance of the solar irradiance from space to the surface was reduced and consequently decreased the solar contribution in the MIR channel. As a result, the correlation of the radiative transfer equations between the MIR and TIR channels of the WiDAS system was higher than that of the MODIS at the same atmospheric conditions. Second, the angular variation of the DBT in both the MIR and TIR channels of the WiDAS system was weakened, which caused the retrieved result to be more sensitive to the noise included in the used DBT data. However, as shown in Fig. 8(b), approximately 80% and 88% of the residual error was respectively within  $[-0.015, 0.015]$  and  $[-0.02, 0.02]$ , which indicates that most of the retrieved error of the MIR reflectivity and TIR emissivity for the WiDAS system was smaller than 0.02 in theory. Fig. 8(c) and (d) shows the histograms of the residual error for the directional effective temperature  $T_e$  calculated from the inversion of the radiative transfer equation using the retrieved TIR emissivity with true DBT and downward atmospheric radiance, and with noise-added DBT and downward atmospheric radiance, respectively. The results were very similar to the results observed with MODIS, as shown in Fig. 7(b) and (c).

#### IV. APPLICATION TO WiDAS AIRBORNE DATA

An airborne multiangular image data set was acquired by the WiDAS system, which was one of the major airborne sensors used in the WATER synthetic field campaign conducted in the spring to summer of 2008 on the Heihe River watershed in West China [29]. The WiDAS system acquired images using four charge-coupled device (CCD) cameras in visible/near-infrared (VNIR) channels and two thermal cameras in the MIR and TIR channels [27], [40]. Table V lists the specification of those cameras. The VNIR image will be used for results analysis.

TABLE VI  
COEFFICIENTS FROM OBSERVED TEMPERATURE OF THE MIR AND TIR CHANNELS TO BLACKBODY BRIGHTNESS TEMPERATURE

	$B_0$	$B_1$	$B_2$
MIR	$2.87597 \times 10^{-2}$	-0.58336	0.00202
TIR	86.19557	0.62729	$2.54228 \times 10^{-4}$

#### A. Acquisition of Multiangular Images

The WiDAS system was designed to observe the surface in the MIR and TIR channels at a total of seven zenith angles (see angle case 4 in Table IV). The cameras of the WiDAS system acquired the surface sequential images with high frequency during the flight [27], and the overlap between two sequential images was more than 80% for the VNIR channels and more than 85% in the MIR and TIR channels, which meant that the same ground point can be almost simultaneously observed in several sequential images. After geometric corrections, a multiangular data set was obtained from the collections of the same ground point in the sequential WiDAS images.

However, because the time interval between two sequential images was very short ( $< 4$  s), the variations of VZA and even VAA were consequently very small, causing the two sequential observations to contain no more angular information about the surface than only one observation did, and the error in the additional observations might influence the final solution of the retrieval. Therefore, we should only use those observations whose VZAs were equal or close to the designed angles. However, because the multiangular images were obtained from sequential observations at the manner of the central projection, which reduced the angular differences between sequential observations for those pixels far from the central line in the cross-track direction, only the pixels on the central line of the camera along the flight track can be observed with the designed angles. Moreover, for the edge pixels in the cross-track direction, their VZAs were almost the same in all sequential images, and only their VAAs changed. To improve the accuracy of the emissivity and temperature retrieval from those pixels, we had to select a group of angular observations with the maximum VZA or VAA difference from the sequential images, with a constraint that the VZA interval between any two angular observations with a similar VAA, or the VAA interval between any two observations with a similar VZA, must be beyond a threshold value, such as 6 $^\circ$  for VZA and 15 $^\circ$  for VAA. Therefore, the emissivity and temperature for different pixels were actually retrieved with different combinations of VAA and VZA, rather than the designed combination.

#### B. Calibration and Atmospheric Correction

The recorded temperatures of the MIR and TIR channels were calibrated to blackbody brightness temperatures using a polynomial approximation as follows:

$$BBT = B_0 + B_1 \cdot T_{\text{obs}} + B_2 \cdot T_{\text{obs}}^2 \quad (14)$$

where  $B_0$ ,  $B_1$ , and  $B_2$  are coefficients, which were regressed from their measurement on a blackbody (Series no. Mikron

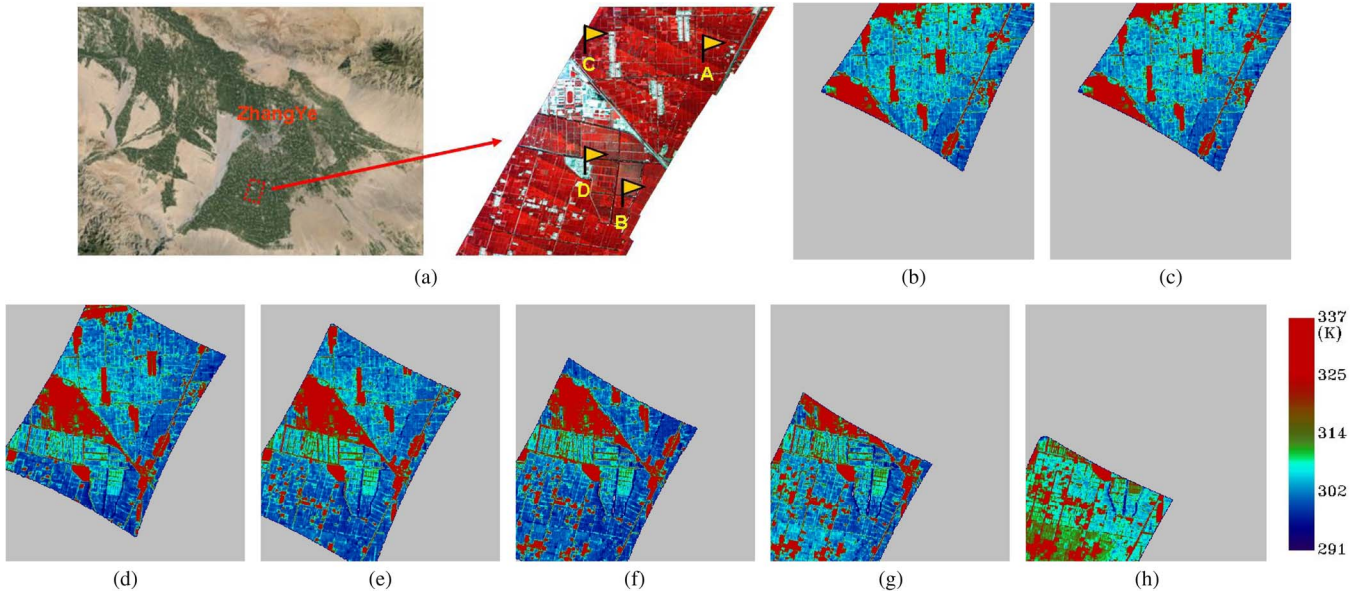


Fig. 9. (a) Study region (38.84°N–38.87°N, 100.39°E–100.43°E) in the Heihe river watershed and its VNIR image from a CCD camera. (b)–(h) Multiangular TIR images. (a) Study region and VNIR image from a CCD camera. (b) Backward 40°. (c) Backward 20°. (d) Backward 10°. (e) Nadir. (f) Forward 10°. (g) Forward 20°. (h) Forward 40°.

340) in the temperature range from 273.16 to 358.16 K with an interval of 5 K. The value of those coefficients is shown in Table VI [40].

For the atmospheric correction of the WiDAS images, radiosounding data, including air temperature, air pressure, relative humidity, and other parameters, were collected simultaneously and used to drive the MODTRAN4.0 code to remove atmospheric effects for the VNIR images and to simulate the upward and downward atmospheric radiance (i.e.,  $R_{a\uparrow}$ , and  $R_{a\downarrow}$ ) and solar radiation (i.e.,  $E_{\text{sun}}$ ,  $R_{\text{sl}\uparrow}$ , and  $R_{\text{sl}\downarrow}$ ) for both MIR and TIR channels. After atmospheric correction, only surface-leaving radiances [i.e.,  $R(\theta_s, \theta_v, \varphi)$  in (2)] were included in the MIR and TIR data.

### C. Directional Emissivity and Effective Temperature

1) *Multiangular Image Data Set*: The study region of this paper is the Zhangye-Yingke-Huazhaizi (ZY-YK-HZZ) experimental site [38.84° N–38.87° N, 100.39° E–100.43° E; see Fig. 9(a)] located in the Heihe River watershed, Zhangye, Gansu, China. This region is a typical oasis agricultural area with a size of about 533 ha, and the main land covers included maize, wheat, and vegetables [27], [29]. The WiDAS system acquired data over this area on June 1, June 29, and July 7, 2008. Only the data from July 7, 2008 were applied because of its clear sky and high quality. Fig. 9(b)–(h) display several sequential images of the DBT in the TIR channel, and those images were acquired at approximately 3:58 UTC (Beijing time: 11:58, duration < 30 s) on July 7, 2008. The solar zenith and azimuth angles at that time were approximately 125.7° and 24.4°, respectively. Because the aircraft flew from northeast to southwest at a height of approximately 1.5 km above the surface, the spatial resolutions of the MIR/TIR cameras and the VNIR images from a CCD camera [see Fig. 9(a)] were approximately 7.9 and 1.25 m, respectively. The red pixels of

TABLE VII  
SPECIFICATION OF FOUR SITES AND THEIR RETRIEVED  
BRDF COEFFICIENTS AND TISIE

No.	Land cover	Lon/Lat	$f_{\text{geo}}$	$f_{\text{vol}}$	$f_{\text{iso}}$	TISIE
Site A	maize	100.411E, 38.857N	0.075	-0.041	0.137	0.978
Site B	orchard	100.402E, 38.844N	0.052	-0.036	0.134	0.971
Site C	wheat	100.398E, 38.859N	0.057	-0.038	0.135	0.974
Site D	barren	100.398E, 38.847N	0.054	0.027	0.150	0.961

the false color image on the right-hand side in Fig. 9(a) represented the vegetated pixels, and the rest were the nonvegetated pixels, such as bare soil, buildings, and man-made road. Four sites composed of  $4 \times 4$  pixels were chosen for further analysis, and their detailed information can be found in Table VII.

From the TIR images in Fig. 9, the difference of pixels' DBTs was up to 46 K. Fig. 10 (see filled circles) shows the DBT after atmospheric correction for four sites shown in the VNIR image in Fig. 8. The changes in VZA (and/or VAA) lead to a temperature variation of approximately 1.0 K, 3.1 K, 2.7 K, and 4.4 K for Sites A, B, C, and D, respectively. Although the DBT difference of Site A was much smaller than that of the other sites, these angular temperature differences were still used for separating emissivity and temperature. Furthermore, the data presented in Fig. 10 also indicated that the higher DBTs were observed at smaller VZAs, whereas the lower DBTs were obtained at larger VZAs because, for the vegetated canopy, the fractions of soil with higher temperature were generally

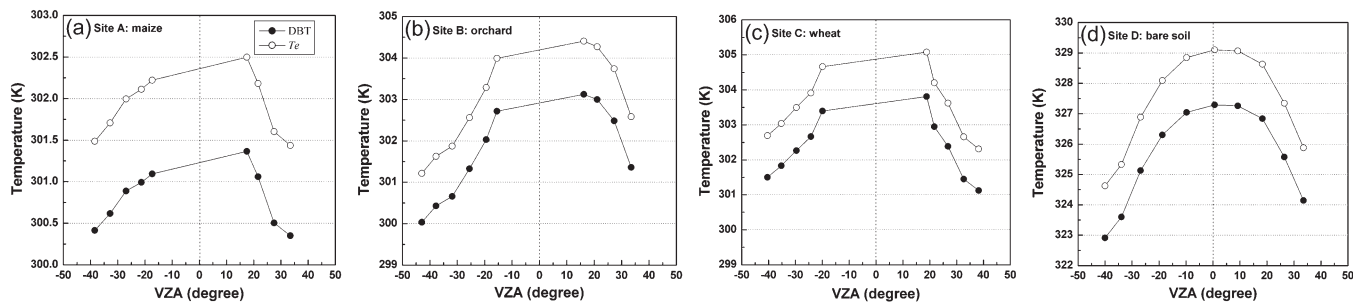


Fig. 10. Angular variation of the measured DBT (filled circles) after atmospheric correction and the effective temperature  $T_e$  (unfilled circles) defined in (12) for four sites. The positive and negative VZAs correspond to nearly opposite VAAs.

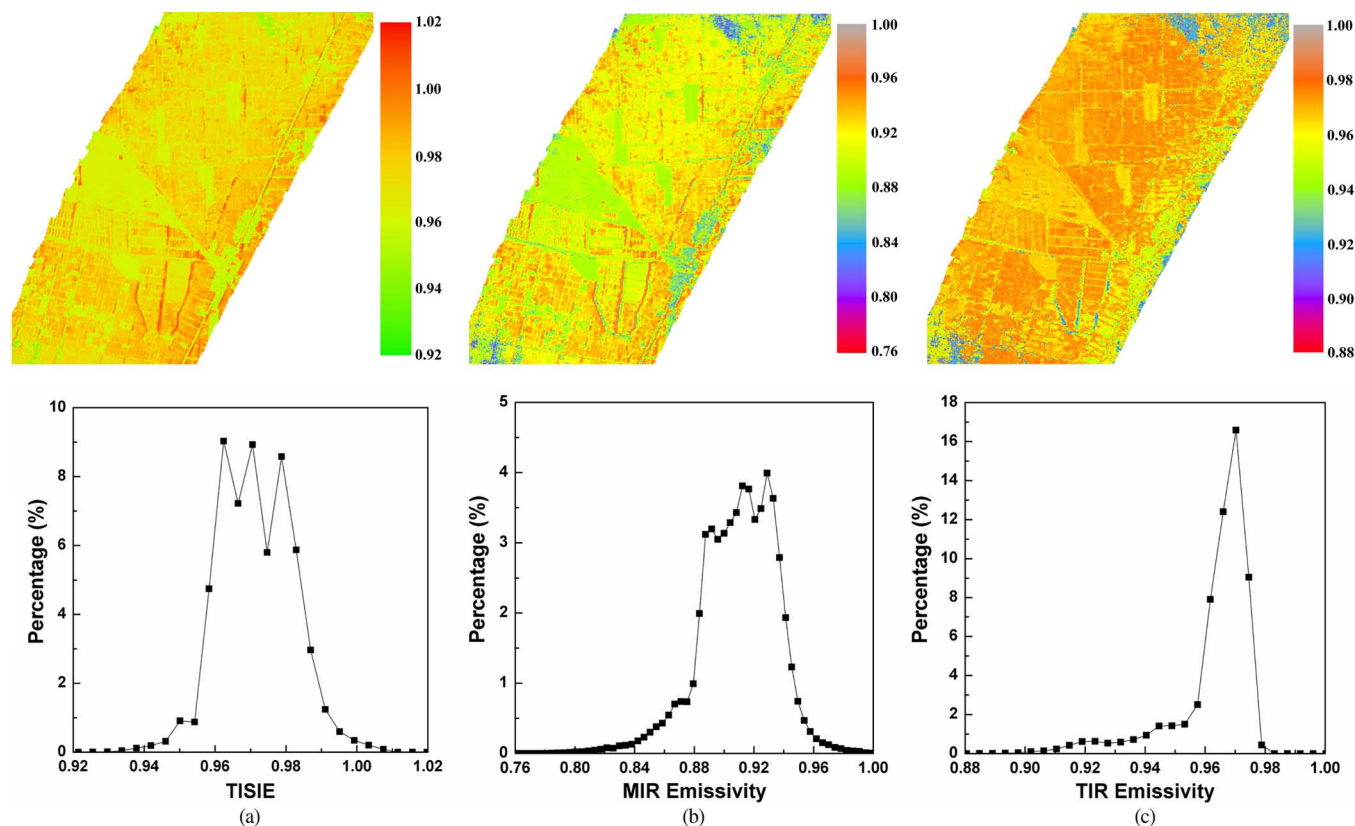


Fig. 11. Retrieved TISIE and nadir emissivities of the MIR and TIR channels. (a) TISIE and its histogram. (b) MIR nadir emissivity and its histogram. (c) TIR nadir emissivity and its histogram.

larger in small VZAs than those in large VZAs. In addition, as reported by some previous studies [46], [47], the bare soil emissivity decreased with the increasing VZA, which most likely caused the soil’s brightness temperature to decrease with the increasing VZA. In addition, note that because all sites, except for Site D, were not located near the central line of the flight track, their minimum VZA was not equal to  $0^\circ$ , as shown in Fig. 10.

2) *Retrieval of Emissivity and Temperature:* Fig. 11 presents the retrieved TISIE and nadir emissivity of the MIR and TIR channels and their histograms. Compared with the region shown in Fig. 9, the region in Fig. 11 is smaller because some of the pixels that could not meet the requirement of the angle interval between different VZAs and VAAs, particularly for those pixels near the edge in the cross-track direction, were removed during the retrieval process. As observed in

Fig. 11(a), the TISIE mainly distributed in the range of [0.95, 1.01], which is similar to the results in [31]. According to the VNIR image in Fig. 9, the TISIE values of vegetated pixels were generally higher than those of bare soil and buildings because the vegetation component in the pixel increased the TISIE values [48].

Similar to the TISIE, both the MIR and TIR emissivities of vegetated pixels were higher than those of nonvegetated pixels, as shown in Fig. 11(b) and (c). However, the emissivity of the MIR channel was generally lower than that of the TIR channel, particularly for the nonvegetated pixels, and the MIR emissivity difference between the vegetated and nonvegetated pixels was larger than that of the TIR emissivity. These results might be due to the fact that most soils and man-made materials present a strong spectral emissivity variation in the range of  $3\text{--}6\ \mu\text{m}$  (“atmospheric window” mainly around  $3.9\ \mu\text{m}$ ), and

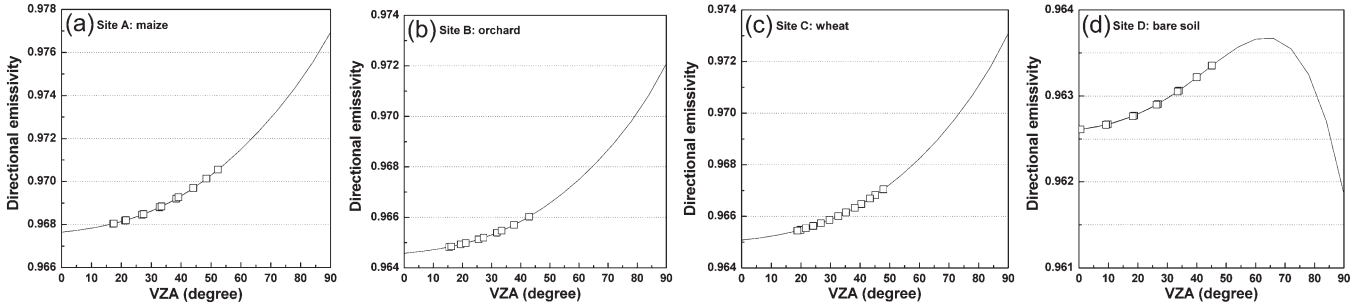


Fig. 12. Directional TIR emissivity for several cover types. The solid line presents the emissivity in all VZAs ( $0^\circ$ – $90^\circ$ ) calculated from (9) using the retrieved BRDF coefficients and TISIE, whereas the squares are the emissivity for those VZAs under which the sites were observed.

the minimum emissivity in this spectral range can be as low as 0.7. Meanwhile, the emissivity of most vegetation in this spectral range was almost flat. In contrast, the spectral emissivity for most land covers (except some soils, rocks, and deserts) is almost flat in the TIR range (e.g., 8–14  $\mu\text{m}$ ), and their values are usually larger than 0.95. The histogram in Fig. 11(b) reveals that the retrieved MIR emissivity mainly ranged from 0.88 to 0.94. Compared with the findings in [22], where the angular emissivities for several types of land cover from MODIS emissivity products were obtained, this emissivity range had the same levels for grass and barren land and was only slightly smaller (approximately 0.005) than the latter for cropland. The TIR emissivity shown in the histogram in Fig. 11(c) is mainly distributed in the range of [0.96, 0.98], which is narrower than the range of the MIR emissivity due to two factors: first, as previously stated, both soil and vegetation emissivities in the TIR range were very high, and their differences in such ranges were smaller than that in the MIR range; second, (9) might reduce the range of the TIR emissivity, particularly for those pixels with a TISIE larger than 1.0.

The angular variations of the TIR emissivity for the aforementioned four sites are presented in Fig. 12. The solid lines are the emissivity of VZAs within  $[0^\circ, 90^\circ]$  that was estimated using the retrieved three coefficients of the BRDF model and TISIE, whereas the squares are the emissivity for those VZAs under which the sites were observed. These results indicate that the directional emissivity for the three vegetated samples increased with VZA, and the emissivity difference between nadir and horizontal (i.e.,  $\text{VZA} = 90^\circ$ ) observations was approximately 0.008 in theory. However, this difference turned out to be as small as 0.004 between nadir and  $\text{VZA} = 60^\circ$  and can almost be ignored for the VZAs varying from nadir to  $\text{VZA} = 40^\circ$ . The angular variation of the emissivity of bare soil (Site D) was quite different from that of those vegetated samples. First, the emissivity increased with the increasing VZA and then decreased at the larger VZAs. Comparisons of the three BRDF coefficients in Table VII indicate that the positive coefficient  $f_{\text{vol}}$  produced a different angular pattern for soil emissivity. If the barren pixels were assumed to be isotropic, there would be no difference among the emissivity and brightness temperatures observed at different VZAs, and the BRDF coefficients  $f_{\text{geo}}$  and  $f_{\text{vol}}$  should be zero. However, because the DBT of Site D varied significantly with the viewing angle [see Fig. 10(d)], perhaps due to the roughness and the multiple shadowing effect of itself, the D-TISI method proposed in this

paper finally produced an optimal solution for the three BRDF coefficients and TISIE, which had the minimum residual error of the radiative transfer equation, without considering the types of land cover. Generally, the angular variation of the barren soil can be ignored because the emissivity difference was as small as 0.002. One should note that not all vegetated pixels have the similar angular patterns, as shown in Fig. 12(a)–(c), and not all nonvegetated pixels have similar angular pattern as Fig. 12(d).

Using the directional emissivity shown in Fig. 12 and the DBT shown in Fig. 10 (see filled circles), the directional effective temperatures  $T_e$  defined by (13) were consequently determined by removing the downward atmospheric radiance from the surface-leaving thermal radiance (see (2), where  $R_{\text{sl}\downarrow}$  and  $E_{\text{sun}}$  are equal to 0 for the TIR channel), and presented in Fig. 10 (see unfilled circles).  $T_e$  was generally larger than DBT after removing the reflected downward atmospheric and nonunity effect of the emissivity mainly because the blackbody emission of the surface was larger than the atmospheric emission. The average differences between  $T_e$  and DBT were approximately 1.1 K, 1.6 K, 1.2 K, and 1.8 K for the four sites, respectively, and Site D (bare soil) had the maximum temperature difference because it had the smallest emissivity, which caused the largest value of the reflected downward atmospheric radiance.

3) *Angular Normalization of Temperature*: As shown in Fig. 10, the surface directional effective temperature  $T_e$  varied with the VZAs and even with the VAAs because the sun-target-sensor viewing geometry determined the fractions of different components with different temperatures in the pixel. As a result, this angular effect made the temperature of different pixels in the same image incomparable because they were observed at different directions, which can produce nonrepresentative results. Therefore, it was very crucial to normalize the retrieved effective temperature at various VZAs to a reference VZA (e.g., at nadir).

Unfortunately, no existing study on the angular normalization of temperature has been previously reported. According to the findings in the literature [49], we modified the kernel-driven BRDF model addressed in (6) by replacing the bidirectional reflectivity with the directional effective temperature  $T_e$  as follows:

$$T_e(\theta_s, \theta_v, \varphi) = f'_{\text{iso}} + f'_{\text{vol}} \cdot k_{\text{vol}}(\theta_s, \theta_v, \varphi) + f'_{\text{geo}} \cdot k_{\text{geo}}(\theta_s, \theta_v, \varphi). \quad (15)$$

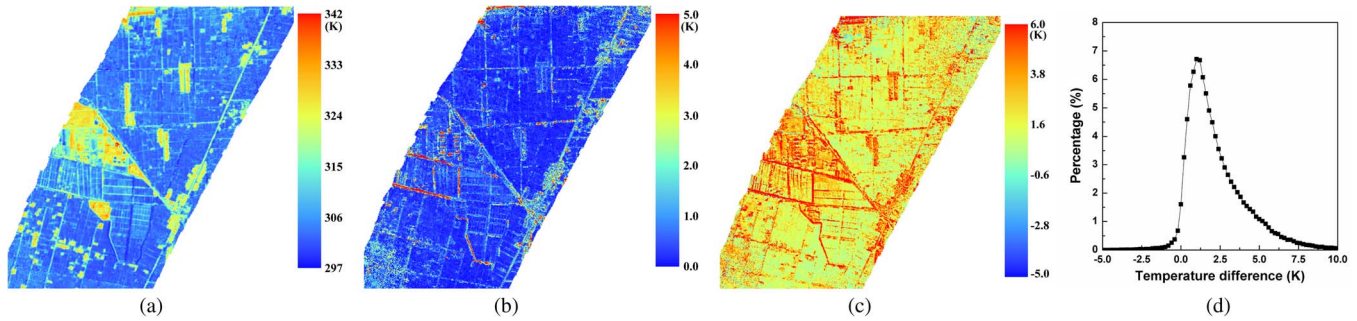


Fig. 13. (a) Nadir effective temperature from the BRDF model ( $T_e$ -nadir). (b) RMSE of the BRDF model for the directional effective temperature. (c) Difference between the nadir effective temperature and the minimum effective temperature of observations. The color scalar was restricted to 6 K, and those pixels with a larger value were forced to 6 K for illustration. (d) Histogram of (c).

The terms in (15) have similar meanings to the discussions in previous sections. To fit the three coefficients  $f'_{iso}$ ,  $f'_{vol}$ , and  $f'_{geo}$ , at least three  $T_e$  values are required. As previously stated, four or more angular observations are needed to solve the four unknowns included in (7), and the retrieval process finally generates a  $T_e$  for each direction, whose number is equal to that of the observations and larger than three. Therefore, the three coefficients in (15) can be fitted in theory as long as the four unknowns in (7) are mathematically solvable. From this point of view, we first used the retrieved directional emissivity in the TIR channel to calculate  $T_e$  at different directions and then fit the three coefficients  $f'_{iso}$ ,  $f'_{vol}$ , and  $f'_{geo}$  and finally extracted the  $T_e$ -nadir from (15). Fig. 13(a) shows the  $T_e$ -nadir of the study area. In addition, to investigate the performance of the BRDF model, the temperature RMSE of this model was also calculated using (16) and displayed in Fig. 13(b), as follows:

$$RMSE = \sqrt{\sum_{k=1}^N [T_e(k) - T_e(k)']^2 / N}, \quad N \geq 4 \quad (16)$$

where  $N$  is the number of angular observations on the same target, and  $T_e(k)$  is the  $k$  th directional effective temperature retrieved from the  $k$  th observation [see (13)], whereas  $T_e(k)'$  is the fitted  $k$  th directional effective temperature from the BRDF model [see (15)].

As shown in Fig. 13(b), the BRDF model produces an error smaller than 1.0 K for most pixels, particularly the vegetated pixels. In contrast, this model produced a significant error (even larger than 3 K) for some nonvegetated pixels, particularly for those nonvegetated pixels near the edge of the image, perhaps because the angle intervals of different observations over those pixels were relatively smaller than the others, which caused the BRDF model to be more sensitive to the error included in the input  $T_e$  and viewing angles, and also possibly because the BRDF model is not representative for those kinds of bare surfaces. However, the BRDF model performed generally well for most pixels in the angular normalization of their directional effective temperature. Fig. 13(c) presents the temperature difference between the nadir effective temperature  $T_e$ -nadir and the minimum value of the effective temperature under different viewing directions, and Fig. 13(d) shows the corresponding histogram in Fig. 13(c), at a step of 0.2 K. To make the data in

Fig. 13(c) more distinguishable, the color scalar of the figure was restricted to 6 K, and those pixels with a larger value were forced to 6 K for illustration purposes. Both Fig. 13(c) and (d) indicate that  $T_e$ -nadir was larger than the minimum temperatures for most pixels (approximately 98%), and their differences mainly fell into the range of [0.0, 5.0] K. Because the temperature difference for most vegetated pixels was in the range of [0.5, 2.0] K, the angular normalization of temperature appeared unnecessary for those pixels if the accuracy of the retrieved temperature is not required to be better than that range. The temperature difference of the nonvegetated pixels was generally larger than that of the vegetated pixels and even exceeded 6.0 K for some cases. Although the BRDF model might cause remarkable temperature error for the nonvegetated pixels, as previously stated, the results for some pixels, such as the barren pixels near Site D in Fig. 9, with which the BRDF model displayed high accuracy, still illustrated that its angular normalization was strongly required for their temperatures because the temperature difference of those pixels was up to several kelvin and far from the maximum tolerance of the temperature retrieval accuracy.

4) *Cross-Comparison With ASTER Emissivity*: Unfortunately, there was no ground-measured emissivity and temperature data available for the validation of the aforementioned results. Cross-comparison with satellite data (such as ASTER) was consequently conducted. ASTER generates surface emissivity products in five TIR channels (CH10: 8.13–8.48  $\mu\text{m}$ ; CH11: 8.48–8.83  $\mu\text{m}$ ; CH12: 8.93–9.28  $\mu\text{m}$ ; CH13: 10.25–10.95  $\mu\text{m}$ ; CH14: 10.95–11.65  $\mu\text{m}$ ) that are retrieved by using the TES algorithm [9]. Because of its relatively finer resolution (approximately 90 m), the ASTER emissivity data provide us an opportunity to make cross-comparisons with the WiDAS TIR emissivity data. To remove the influence of the spectral differences between the ASTER and WiDAS TIR channels, we established a linear relationship to convert the emissivity of the five ASTER channels to that of the WiDAS TIR channel by using the method described in [50] and more than 100 emissivity spectra, including vegetation, soil, and water samples, chosen from UCSB emissivity database. Finally, the linear relationship is expressed as

$$\bar{\varepsilon} = 0.129 \cdot \varepsilon_{10} - 0.010 \cdot \varepsilon_{11} + 0.193 \cdot \varepsilon_{12} + 0.628 \cdot \varepsilon_{13} + 0.060 \cdot \varepsilon_{14} \quad (17)$$

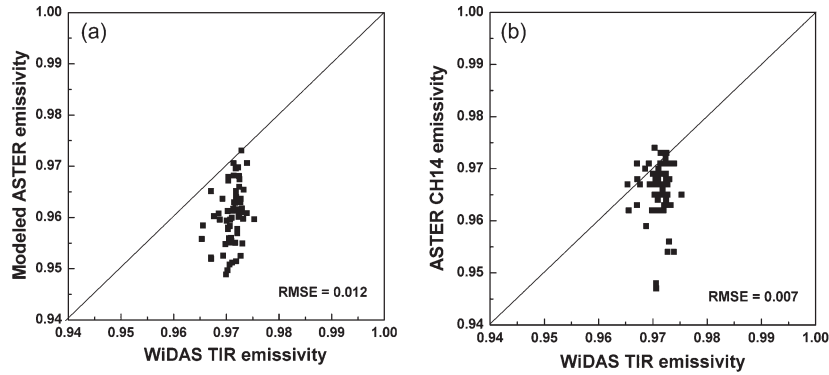


Fig. 14. (a) WiDAS TIR emissivity and modeled ASTER emissivity from (17). (b) WiDAS TIR emissivity with ASTER channel 14 emissivity.

where  $\varepsilon_k (k = 10, 11, \dots, 14)$  is the  $k$ th channel's ASTER emissivity. The fitted emissivity RMSE of the aforementioned linear relationship is less than 0.003. The ASTER sensor observed the study area on June 29, 2008. However, there were only 65 clear-sky pixels that had valid emissivity due to the occurrence of clouds. Fig. 14(a) shows the comparison of the average WiDAS TIR emissivity aggregated from 7.9 to 90 m and the modeled ASTER emissivity  $\bar{\varepsilon}$  from (17). The comparison indicates that the WiDAS emissivity was, in total, higher than the modeled ASTER emissivity  $\bar{\varepsilon}$ , with an RMSE of approximately 0.012. In addition, the WiDAS emissivity and ASTER channel 14 (10.8–11.8  $\mu\text{m}$ ) emissivity were relatively closer to each other, as shown in Fig. 14(b), but still with an RMSE of approximately 0.007.

The difference between the ASTER and WiDAS emissivities might be caused by the intrinsic difference of their algorithms, the temporal variation of the emissivity itself from June 29 to July 7, 2008, as well as the spatial scale effect of the two products. However, as reported by some previous studies, the TES algorithm suffers from spectral emissivity contrast with dense vegetation surfaces [51]–[55] and consequently introduces more uncertainty into the retrieved emissivity of those surfaces. According to the results in [56], which found that the ASTER emissivity was 0.01–0.02 smaller than the MODIS emissivity retrieved using the day/night algorithm [13], and the results reported in Fig. 14(a), the WiDAS TIR emissivity might be closer to the MODIS emissivity. However, it is almost impossible to perform cross-comparison with the MODIS data because of the coarser resolution (approximately 6 km in Collection 5).

## V. CONCLUSION AND DISCUSSIONS

This paper has proposed a D-TISI method to retrieve directional emissivity and effective temperature from daytime multiangular observed images in both MIR and TIR channels by combining the kernel-driven BRDF model and the TISI method. In contrast to most previous studies, the nonisothermal surface/canopy was a concern. For model analysis, the canopy's bidirectional reflectivity and emissivity in the MIR and TIR channels were simulated using the SAILH model, and the canopy's DBT and radiance were simulated as the weight average of components' temperatures and their fractions calculated from a parameterization of the SAILH model in [45]. Two

groups of MIR and TIR channels were used for illustration, and they were respectively from the MODIS that had narrow bandwidths and is more representative of current most sensors and from the airborne WiDAS system that, in contrast, had much boarder bandwidths and whose data were used for validating the D-TISI method. Four groups of angular combinations were designed to investigate the influence of the angular observations on the retrieval accuracy. Generally, large angle intervals among the angular observations and a larger VZA with respect to nadir direction can improve the retrieval accuracy of emissivity and temperature because those angle conditions result in significant variation of components' fractions and DBT under different viewing directions. The influences of canopy LAI, components' temperatures, and TISIE on the retrieval accuracy were also discussed. The results generally indicated that, for DBT noise within  $[-1.0, 1.0]$  K and atmospheric data noise within  $[-10\%, 10\%]$ , the D-TISI method can obtain emissivity and temperature with an accuracy within 0.015 and 1.5 K for the MODIS channels and within 0.02 and 1.5 K for the WiDAS channels, respectively.

We applied the D-TISI method to retrieve directional emissivity and effective temperature from the multiangular MIR and TIR images acquired by the airborne WiDAS system at the Heihe River watershed. The results indicated that the vegetated pixels had larger TISIE values and emissivity than the nonvegetated pixels. The retrieved angular variation of the directional emissivity for the vegetated sites from nadir to the horizontal direction was approximately 0.01, which is larger than that of the bare soil site. A comparison with the ASTER emissivity product at the study area showed that the difference of the retrieved nadir emissivity and the ASTER emissivity was approximately 0.012. Furthermore, we used the kernel-driven BRDF model by replacing the bidirectional reflectivity in the original model with the retrieved directional effective temperature  $T_e$  to normalize  $T_e$  from the off-nadir direction to the nadir. The results indicate that the temperature difference between the normalized nadir effective temperature ( $T_e$ -nadir) and the minimum  $T_e$  of the observing directions was 0.5–2.0 K for most vegetated pixels and always several kelvin for most nonvegetated pixels. Therefore, it is necessary to perform angular normalization on LST measurements for higher accuracy. However, the retrieved nadir and off-nadir effective temperatures were not validated in this paper due to the lack of field data.



Note that the LST also displays temporal variation, except for angular variation, due to the fluctuations of the local meteorological and solar conditions, and this temporal variation is sometimes more significant than the angular variation. However, this paper ignored this temporal variation and considered the temperature variation fully caused by the changes of viewing angles because, up to now, there has been no operational method developed to allow time normalization of measured DBT data from multiangular observations and also because the time interval between the two sequential images examined in this paper was very short ( $< 4$  s). However, we should keep in mind that the lack of consideration of the temporal variation must have degraded the retrieval accuracy. In addition, different VZAs corresponded to ground pixels with different areas, which might cause the pixels observed on the same place to include different components, particularly for the heterogeneous surfaces. This problem, along with the misregistration between different images, might have led to more uncertainty in the retrieval results. Moreover, although we discussed the influence of the angular combination on the retrieval accuracy only from four groups of angles (see Table IV) and chose angle case 2 as the local optimum combination among those groups, the conclusions based on those angle cases are limited and additional investigation is required in the future to determine the global optimum combination in the upper hemisphere.

In addition, the results of the model analysis in Section III-F were only suitable for the pixels in the central line of the images along the flight track because the angular combination for those pixels far from this central line in the central projection image or linear-array detecting system was actually different from the designed angular combination and their angle intervals were consequently significantly reduced. As a result, the retrieval accuracy gradually decreased, in theory, for the pixels moving from the central line to the edge. A sensor with the conical scanning method, such as the Advanced Microwave Scanning Radiometer for EOS (AMSR-E, [http://aqua.nasa.gov/about/instrument\\_amsr.php](http://aqua.nasa.gov/about/instrument_amsr.php)), is expected in the future to ensure that all pixels have the same angular combinations.

Furthermore, since the D-TISI method requires the multiangular observation in MIR and TIR channels, it cannot be applied to any current satellite sensor that is unable to provide such multiangular images. Therefore, the D-TISI method remains in the methodological domain in the current status. However, we can prospect that the D-TISI method is applicable to the geostationary satellite data on the basis of two factors: First, a geostationary satellite measures the same place at a high time frequency, and the components' fractions vary with the movement of the solar position in one day; as a result, the fixed viewing angle may also provide similar information of the multiangular measurements. Second, the D-TISI method actually does not need those multiangular images acquired simultaneously as long as the atmospheric correction is operational and the emissivity of the pixel keeps stable in the short period. In addition, we hope that the local optimal angular combination obtained from the sensitivity analysis of the D-TISI method can provide some suggestions for the future design of the airborne or spaceborne thermal sensor with multiangular observation system.

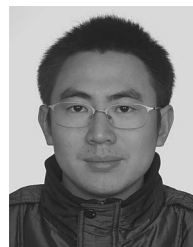
## ACKNOWLEDGMENT

The authors would like to thank the two anonymous reviewers for their constructive and thoughtful comments and suggestions and the colleagues who collected the data set of the multiangular MIR and TIR data.

## REFERENCES

- [1] W. G. M. Bastiaanssen, M. Menenti, R. A. Feddes, and A. A. M. Holtslag, "A remote sensing surface energy balance algorithm for land (SEBAL). I. Formulation," *J. Hydrol.*, vol. 212/213, pp. 198–212, 1998.
- [2] J. Hansen, R. Ruedy, M. Sato, and K. Lo, "Global surface temperature change," *Rev. Geophys.*, vol. 48, no. 4, p. RG4004, Dec. 2010.
- [3] Q. Weng, "Thermal infrared remote sensing for urban climate and environmental studies: Methods, applications, and trends," *ISPRS J. Photogramm. Remote Sens.*, vol. 64, no. 4, pp. 335–344, Jul. 2009.
- [4] Z. Qin, A. Karnieli, and P. Berliner, "A mono-window algorithm for retrieving land surface temperature from Landsat TM data and its application to the Israel-Egypt border region," *Int. J. Remote Sens.*, vol. 22, no. 18, pp. 3719–3746, 2001.
- [5] J. C. Jiménez-Muñoz and J. A. Sobrino, "A generalized single-channel method for retrieving land surface temperature from remote sensing data," *J. Geophys. Res.*, vol. 108, no. D22, p. 4688, Nov. 2003.
- [6] F. Becker and Z.-L. Li, "Towards a local split window method over land surfaces," *Int. J. Remote Sens.*, vol. 11, no. 3, pp. 369–393, 1990.
- [7] F. Becker and Z.-L. Li, "Surface temperature and emissivity at various scales: Definition, measurement and related problems," *Remote Sens. Rev.*, vol. 12, no. 3/4, pp. 225–253, 1995.
- [8] Z. Wan and J. Dozier, "A generalized split-window algorithm for retrieving land-surface temperature from space," *IEEE Trans. Geosci. Remote Sens.*, vol. 34, no. 4, pp. 892–905, Jul. 1996.
- [9] A. Gillespie, S. Rokugawa, T. Matsui, J. S. Cothren, S. Hook, and A. B. Kahle, "A temperature and emissivity separation algorithm for Advanced Spaceborne Thermal Emission and Reflection Radiometer (ASTER) images," *IEEE Trans. Geosci. Remote Sens.*, vol. 36, no. 4, pp. 1113–1126, Jul. 1998.
- [10] F. Becker and Z.-L. Li, "Temperature-independent spectral indices in thermal infrared bands," *Remote Sens. Environ.*, vol. 32, no. 1, pp. 17–33, Aug. 1990.
- [11] K. Watson, "Two-temperature method for measuring emissivity," *Remote Sens. Environ.*, vol. 42, no. 2, pp. 117–121, Nov. 1992.
- [12] L. F. Peres and C. C. DaCamara, "Land surface temperature and emissivity estimation based on the two-temperature method: Sensitivity analysis using simulated MSG/SEVIRI data," *Remote Sens. Environ.*, vol. 91, no. 3/4, pp. 377–389, Jun. 2004.
- [13] Z. Wan and Z.-L. Li, "A physics-based algorithm for retrieving land-surface emissivity and temperature from EOS/MODIS data," *IEEE Trans. Geosci. Remote Sens.*, vol. 35, no. 4, pp. 980–996, Jul. 1997.
- [14] P. M. Ingram and A. H. Muse, "Sensitivity of iterative spectrally smooth temperature/emissivity separation to algorithmic assumptions and measurement noise," *IEEE Trans. Geosci. Remote Sens.*, vol. 39, no. 10, pp. 2158–2257, Oct. 2001.
- [15] P. S. Kealy and S. J. Hook, "Separating temperature and emissivity in thermal infrared multispectral scanner data: Implications for recovering land surface temperatures," *IEEE Trans. Geosci. Remote Sens.*, vol. 31, no. 6, pp. 1155–1164, Nov. 1993.
- [16] Z.-L. Li, R. Zhang, X. Sun, H. Su, X. Tang, Z. Zhu, and J. A. Sobrino, "Experimental system for the study of the directional thermal emission of natural surfaces," *Int. J. Remote Sens.*, vol. 25, no. 1, pp. 195–204, 2004.
- [17] J. P. Lagouarde, Y. H. Kerr, and Y. Brunnet, "An experimental study of angular effects on surface temperature for various plant canopies and bare soils," *Agri. Forest Meteorol.*, vol. 77, no. 3/4, pp. 167–190, Dec. 1995.
- [18] J.-P. Lagouarde, P. Moreau, M. Irvine, J.-M. Bonnefond, J. A. Voogt, and F. Sollice, "Airborne experimental measurements of the angular variations in surface temperature over urban areas: Case study of Marseille (France)," *Remote Sens. Environ.*, vol. 93, no. 4, pp. 443–462, Dec. 2004.
- [19] P. Minnis and M. M. Khaiyer, "Anisotropy of land surface skin temperature derived from satellite data," *J. Appl. Meteorol.*, vol. 39, no. 7, pp. 1117–1129, Jul. 2000.
- [20] M. O. Rasmussen, F.-M. Göttsche, F.-S. Olesen, and I. Sandholt, "Directional effects on land surface temperature estimation from MeteorSat Second Generation for savanna landscapes," *IEEE Trans. Geosci. Remote Sens.*, vol. 49, no. 11, pp. 4458–4468, Nov. 2011.

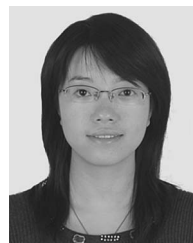
- [21] A. Chehbouni, Y. Nouvellon, Y. H. Kerr, M. S. Moran, C. Watts, L. Prevot, D. C. Goodrich, and S. Rambal, "Directional effect on radiative surface temperature measurements over a semi-arid grassland site," *Remote Sens. Environ.*, vol. 76, no. 3, pp. 360–372, Jun. 2001.
- [22] H. Ren, G. Yan, L. Chen, and Z. Li, "Angular effect of MODIS emissivity products and its application to the split-window algorithm," *ISPRS J. Photogramm. Remote Sens.*, vol. 66, no. 4, pp. 498–507, Jul. 2011.
- [23] H. Ren, G. Yan, R. Liu, F. Nerry, Z.-L. Li, and R. Hu, "Impact of sensor footprint on measurement of directional brightness temperature of row crop canopies," *Remote Sens. Environ.*, vol. 134, pp. 135–151, Jul. 2013.
- [24] Z.-L. Li, M. P. Stoll, R. Zhang, L. Jia, and Z. Su, "On the separate retrieval of soil and vegetation temperatures from ATSR data," *Sci. China Series D*, vol. 44, no. 2, pp. 97–111, Feb. 2001.
- [25] M. Menenti, L. Jia, Z.-L. Li, V. Djepa, J. Wang, M. P. Stoll, Z. Su, and M. Rast, "Estimation of soil and vegetation temperatures with multiangular thermal infrared observations: IMGRASS, HEIFE, and SGP 1997 experiments," *J. Geophys. Res.*, vol. 106, no. D11, pp. 11997–12010, Jun. 2001.
- [26] L. Jia, Z.-L. Li, M. Menenti, Z. Su, W. Verhoef, and Z. Wan, "A practical algorithm to infer soil and foliage component temperatures from biangular ATSR-2 data," *Int. J. Remote Sens.*, vol. 24, no. 23, pp. 4739–4760, 2003.
- [27] Q. Liu, C. Yan, Q. Xiao, G. Yan, and L. Fang, "Separating vegetation and soil temperature using airborne multiangular remote sensing image data," *Int. J. Appl. Earth Observ. Geoinformation*, vol. 17, pp. 66–75, Jul. 2012.
- [28] W. Zhan, Y. Chen, J. Zhou, and J. Li, "An algorithm for separating soil and vegetation temperatures with sensors featuring a single thermal channel," *IEEE Trans. Geosci. Remote Sens.*, vol. 49, no. 5, pp. 1796–1809, May 2011.
- [29] X. Li, X. Li, Z. Li, M. Ma, J. Wang, Q. Xiao, Q. Liu, T. Che, E. Chen, G. Yan, Z. Hu, L. Zhang, R. Chu, P. Su, Q. Liu, S. Liu, J. Wang, Z. Niu, Y. Chen, R. Jin, W. Wang, Y. Ran, X. Xin, and H. Ren, "Watershed Allied Telemetry Experimental Research," *J. Geophys. Res.*, vol. 114, no. D22, p. D22103, Nov. 2009.
- [30] Z.-L. Li, B.-H. Tang, H. Wu, H. Ren, G. Yan, Z. Wan, I. F. Trigo, and J. A. Sobrino, "Satellite-derived land surface temperature: Current status and perspectives," *Remote Sens. Environ.*, vol. 131, pp. 14–37, Apr. 2013.
- [31] C. François, C. Ottlé, and L. Prévot, "Analytical parameterization of canopy directional emissivity and directional radiance in the thermal infrared: Application on the retrieval of soil and foliage temperatures using two directional measurements," *Int. J. Remote Sens.*, vol. 18, no. 12, pp. 2587–2621, 1997.
- [32] C. François, "The potential of directional radiometric temperatures for monitoring soil and leaf temperature and soil moisture status," *Remote Sens. Environ.*, vol. 80, no. 1, pp. 122–133, Apr. 2002.
- [33] F. Petitcolin and F. Nerry, "Mapping temperature independent spectral indices of emissivity and directional emissivity in AVHRR channels 4 and 5," *Int. J. Remote Sens.*, vol. 23, no. 17, pp. 3473–3491, 2002.
- [34] Z.-L. Li, F. Petitcolin, and R. Zhang, "A physically based algorithm for land surface emissivity retrieval from combined mid-infrared and thermal infrared data," *Sci. China Series E, Technol. Sci.*, vol. 43, no. 1, pp. 23–33, Dec. 2000.
- [35] G. M. Jiang, Z.-L. Li, and F. Nerry, "Land surface emissivity retrieval from combined mid-infrared and thermal infrared data of MSG-SEVIRI," *Remote Sens. Environ.*, vol. 105, no. 4, pp. 326–340, Dec. 2006.
- [36] K. Goïta and A. Royer, "Surface temperature and emissivity separability over land surface from combined TIR and SWIR AVHRR data," *IEEE Trans. Geosci. Remote Sens.*, vol. 35, no. 3, pp. 718–733, May 1997.
- [37] Z.-L. Li and F. Becker, "Feasibility of land surface temperature and emissivity determination from AVHRR data," *Remote Sens. Environ.*, vol. 43, no. 1, pp. 67–85, Jan. 1993.
- [38] G. M. Jiang and Z.-L. Li, "Intercomparison of two BRDF models in the estimation of the directional emissivity in MIR channel from MSG1-SEVIRI data," *Opt. Exp.*, vol. 16, no. 23, pp. 19310–19321, Nov. 2008.
- [39] F. Nerry, F. Petitcolin, and M. P. Stoll, "Bidirectional reflectivity in AVHRR channel 3: Application to a region in Northern Africa," *Remote Sens. Environ.*, vol. 66, no. 3, pp. 298–316, Dec. 1998.
- [40] L. Fang, Q. Liu, Q. Xiao, Q. Liu, and Z. Liu, "Design and implementation of airborne wide-angle infrared dual-mode line/array scanner in Heihe experiment," *Adv. Earth Sci. (Chinese J. English abstract)*, vol. 24, no. 7, pp. 696–704, 2009.
- [41] W. Verhoef, "Theory of radiative transfer models applied in optical remote sensing of vegetation canopies," Ph.D. dissertation, Wageningen Agricultural Univ., Wageningen, Netherlands, 1989.
- [42] W. Verhoef, "Light scattering by leaf layers with application to canopy reflectance modeling: The SAIL model," *Remote Sens. Environ.*, vol. 16, no. 2, pp. 125–141, Oct. 1984.
- [43] A. Kuusk, "The highest peak effect of a uniform vegetative cover," *Soviet J. Remote Sens.*, vol. 3, pp. 645–658, 1985.
- [44] X. Li, A. H. Strahler, and M. A. Fried, "A conceptual model for effective directional emissivity from nonisothermal surfaces," *IEEE Trans. Geosci. Remote Sens.*, vol. 37, no. 5, pp. 2508–2517, Sep. 1999.
- [45] J. Li, G. Yan, and X. Mu, "A parameterized SAILH model for LAI retrieval," *J. Remote Sens.*, vol. 14, no. 6, pp. 1182–1195, 2010.
- [46] Z.-L. Li, H. Wu, N. Wang, S. Qiu, J. A. Sobrino, Z. Wan, B.-H. Tang, and G. Yan, "Land surface emissivity retrieval from satellite data," *Int. J. Remote Sens.*, vol. 34, no. 9/10, pp. 3084–3127, Jan. 13, 2013.
- [47] J. A. Sobrino and J. Cuenca, "Angular variation of thermal infrared emissivity for some natural surfaces from experimental measurements," *Appl. Opt.*, vol. 38, no. 18, pp. 3931–3936, 1999.
- [48] Z.-L. Li and F. Becker, "Properties and comparison of temperature-independent thermal infrared spectral indices with NDVI for HAPEX data," *Remote Sens. Environ.*, vol. 33, no. 3, pp. 165–182, Sep. 1990.
- [49] J. Peng, Q. Liu, Q. Liu, J.-H. Li, H.-Z. Ma, and L. Fang, "Kernel-driven model fitting of multi-angle thermal infrared brightness temperature and its application," *J. Infrared Milli. Waves*, vol. 30, no. 4, pp. 361–365, 2011.
- [50] H. Ren, S. Liang, G. Yan, and J. Cheng, "Empirical algorithms to map global broadband emissivities over vegetated surfaces," *IEEE Trans. Geosci. Remote Sens.*, vol. 51, no. 5, pp. 2619–2631, May 2013.
- [51] A. R. Gillespie, E. A. Abbott, L. Gilson, G. Hulley, J.-C. Jiménez-Muñoz, and J. A. Sobrino, "Residual errors in ASTER temperature and emissivity standard products AST08 and AST05," *Remote Sens. Environ.*, vol. 115, no. 12, pp. 3681–3694, Dec. 15, 2011.
- [52] S. Yoriko, M. Tsuneko, R. Shuichi, and H. Akira, "Temperature and emissivity separation for multi-band radiometer and validation ASTER TES algorithm," *J. Remote Sens. Soc. Japan*, vol. 23, no. 4, pp. 364–375, 2003.
- [53] W. T. Gustafson, A. R. Gillespie, and G. Yamada, "Revisions to the ASTER temperature/emissivity separation algorithm," in *Proc. 2nd Recent Adv. Quant. Remote Sens.*, Valencia, Spain, 2006, pp. 770–775.
- [54] G. C. Hulley and S. J. Hook, "The North American ASTER Land Surface Emissivity Database (NAALSED) version 2.0," *Remote Sens. Environ.*, vol. 113, no. 9, pp. 1967–1975, Sep. 2009.
- [55] V. Payan and A. Royer, "Analysis of temperature emissivity separation (TES) algorithm applicability and sensitivity," *Int. J. Remote Sens.*, vol. 25, no. 1, pp. 15–37, 2004.
- [56] K. Wang and S. Liang, "Evaluation of ASTER and MODIS land surface temperature and emissivity products using long-term surface longwave radiation observations at SURFRAD sites," *Remote Sens. Environ.*, vol. 113, no. 7, pp. 1556–1565, 2009.



**Huazhong Ren** received the Ph.D. degree from Beijing Normal University, Beijing, China, and from the Université de Strasbourg, Strasbourg, France, in 2013.

He is currently a Postdoctoral Researcher with the Institute of Remote Sensing and Geographic Information System, Peking University, Beijing, China. His current research interests focus on the retrieval of land surface temperature/emissivity and their angular correction. He has also devoted his efforts to the spectral calibration of broadband images for airborne

and spaceborne instruments.



**Rongyuan Liu** is currently working toward the Ph.D. degree at Beijing Normal University, Beijing, China.

During 2012–2013, she was a Visiting Student with the ICube team, Université de Strasbourg, Illkirch, France. Her current research interests focus on the retrieval of the fraction of photosynthetically active radiation from satellite data and its validation.



**Guangjian Yan** received the Ph.D. degree from the Institute of Remote Sensing Applications, Chinese Academy of Sciences, Beijing, China, in 1999.

He is currently a Professor with Beijing Normal University, Beijing, China. He has published more than 100 papers. His main research interests include multiangular and thermal infrared remote sensing.



**Françoise Nerry** received the Ph.D. degree in 1988.

Since 1990, she has been a Permanent Researcher with the Image Sciences, Computer Sciences and Remote Sensing Laboratory (LSIIT), CNRS, Illkirch, France, which changed to ICube in 2013. She is also the Head of the TRIO/ICube team involving 40 persons, including 20 permanents. She has been involved in numerous national and international programs. Her research interests include thermal infrared radiometry and methodology of physical analysis of remote sensing data.



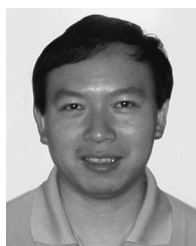
**Xihan Mu** received the Ph.D. degree in remote sensing from the School of Geography, Beijing Normal University, Beijing, China, in 2009.

In 2007, he was a Visiting Student with the Laboratoire des Sciences de l'Images, de l'Informatique et de la Télédétection, Louis Pasteur University, Strasbourg, France. He is currently a Lecturer (Assistant Professor) with the School of Geography, Beijing Normal University. His research interests include using multiangular remote sensing to retrieve vegetation structural parameters and land surface

temperature.

**Zhao-Liang Li** received the Ph.D. degree in 1990.

Since 1992, he has been a Research Scientist with CNRS, Illkirch, France. In 2013, he joined the Institute of Agricultural Resources and Regional Planning, Chinese Academy of Agricultural Sciences, Beijing, China. He has participated in more than 20 national and international projects. He has published more than 100 papers in international refereed journals. His main research interests include thermal infrared radiometry, parameterization of land surface processes at large scale, and assimilation of satellite data to land surface models.



**Qiang Liu** received the B.S. degree in computational mathematics from Peking University, Beijing, China, in 1997 and the Ph.D. degree in cartography and remote sensing from the Institute of Remote Sensing Applications, Chinese Academy of Sciences, Beijing, China, in 2002.

He is currently a Senior Scientist with the College of Global Change and Earth System Science, Beijing Normal University, Beijing, China, and also with the State Key Laboratory of Remote Sensing Science, Institute of Remote Sensing and Digital Earth, Chinese Academy of Sciences, Beijing, China. His main research interest includes multiangular remote sensing, such as geometric processing of multiangular images, bidirectional reflectance distribution function/albedo modeling, and component temperature retrieval.